Naval Research Laboratory
Washington, DC 20375-5320

Extinction Dynamics of a Co-flow Diffusion Flame by Very Small Water Droplets Injected into the Air Stream

RAMAGOPAL ANANTH
RICHARD C. MOWREY

Navy Technology Center for Safety and Survivability
Chemistry Division

July 28, 2008

REPORT DOCUMENTATION PAGE

Form Approved
OMB No. 0704-0188

1. REPORT DATE *(DD-MM-YYYY)*	2. REPORT TYPE	3. DATES COVERED *(From - To)*
28-07-2008	Memorandum Report	

4. TITLE AND SUBTITLE

Extinction Dynamics of a Co-flow Diffusion Flame by Very Small Water Droplets Injected into the Air Stream

5a. CONTRACT NUMBER

5b. GRANT NUMBER

5c. PROGRAM ELEMENT NUMBER

6. AUTHOR(S)

Ramagopal Ananth and Richard C. Mowrey

5d. PROJECT NUMBER

5e. TASK NUMBER

5f. WORK UNIT NUMBER

7. PERFORMING ORGANIZATION NAME(S) AND ADDRESS(ES)

Naval Research Laboratory
4555 Overlook Avenue, SW
Washington, DC 20375-5320

8. PERFORMING ORGANIZATION REPORT NUMBER

NRL/MR/6180--08-9131

9. SPONSORING / MONITORING AGENCY NAME(S) AND ADDRESS(ES)

Office of Naval Research
One Liberty Center
875 North Randolph St.
Arlington, VA 22203-1995

10. SPONSOR / MONITOR'S ACRONYM(S)

11. SPONSOR / MONITOR'S REPORT NUMBER(S)

12. DISTRIBUTION / AVAILABILITY STATEMENT

Approved for public release; distribution is unlimited.

13. SUPPLEMENTARY NOTES

14. ABSTRACT

Computations are performed to examine the effectiveness of mono-disperse water droplets in extinguishing a co-flow, propane diffusion flame by injecting the droplets into the air stream. The calculations show that the droplets entrained into the reaction kernel at the flame base are crucial for extinction. The reaction kernel detaches from the burner rim and blows-off when the droplet concentration is increased to a critical value (extinction concentration). At the critical value, the maximum chain-branching reaction ($H_2+O=OH+H$) rate in the reaction kernel was found to be reduced by a factor of 5 in our computations. A large decrease in the reaction rate indicates that the maximum heat generations rate and Damkholer number are too low to sustain the flame, and cause the flame blow-off. Large drops are more effective than small drops, and the extinction concentration of water increases from 10.5% to 15% by mass as the size is reduced from 32 to 4 micro m. As the droplet size is increased further (>32 micro m), the trend will reverse as the evaporation rates get too small despite increased penetration of flame core by the drops.

15. SUBJECT TERMS

Water mist	Extinction	Cupburner
Propane combustion	Diffusion flame	

16. SECURITY CLASSIFICATION OF:

a. REPORT	b. ABSTRACT	c. THIS PAGE	17. LIMITATION OF ABSTRACT	18. NUMBER OF PAGES	19a. NAME OF RESPONSIBLE PERSON
Unclassified	Unclassified	Unclassified	UL	62	Ramagopal Ananth

19a. NAME OF RESPONSIBLE PERSON
Ramagopal Ananth

19b. TELEPHONE NUMBER *(include area code)*
(202) 767-3197

Standard Form 298 (Rev. 8-98)
Prescribed by ANSI Std. Z39.18

CONTENTS

NOMENCLATURE

A_r	Pre-exponential coefficient in Arrhenius rate for forward reaction, r
C_{Dn}	Drag coefficient for spherical water droplet
$C_{j,r}$	Mass concentration of specie j in reaction r, Kg/m^3
$C_{H2O,s}$	Saturation concentration of water vapor at droplet surface, Kg/m^3
$C_{H2O,n}$	Concentration of water vapor in the gas mixture surrounding the droplet, Kg/m^3
$C_{p,d}$	Specific heat of liquid water, J/KgK
$C_{p,H2O}$	Specific heat of water vapor, J/KgK
$C_{p,i}$	Specific heat of gas specie i, J/KgK
C_{pm}	Specific heat of gas mixture, J/KgK
D_{ij}	Diffusion coefficient of specie i in a binary mixture of species i and j, m^2/sec
D_{im}	Diffusivity of specie i in a gas mixture, m^2/sec
d_{pn}	Droplet diameter, m
Da	Damkohler number
E	Total energy density of gas mixture, J/m^3
E_r	Activation energy of forward reaction r, J/Kgmole
F_d	Gas-liquid coupling term for momentum
Gr	Grashof number
G	Incident radiation intensity, W/m^2
g	Gravity vector
h_{fg}	Latent heat of vaporization of water, J/Kg
h_i	Specific enthalpy of formation of specie i, J/Kgmole
h^0_i	Standard enthalpy of formation of specie i, J/Kgmole
h_{pn}	Heat transfer coefficient for spherical water droplet, W/m^2K
J_i	Diffusion mass transfer flux for specie i, Kg/m^2sec
K_r	Chemical equilibrium constant for reaction r

k_{fr}	Forward kinetic constant for reversible reaction r
k_{br}	Backward kinetic constant for reversible reaction r
k_{pn}	Water vapor mass transfer coefficient for the droplet, m/sec
M_i	Molecular weight of specie i, Kg/Kgmole
$\dot{m}_{pn}$	Evaporation rate of water droplet, Kg/sec
m_{pn}	Mass of water droplet, Kg
N	Total number of species
N_R	Number of chemical reactions
N_r	Number of species in reaction r
Np	Number density of droplets, $\#/m^3$
N^0_p	Number density of droplets in inlet air, $\#/m^3$
Nu_{pn}	Nusselt number for water droplet
p	Pressure, Newtons/m^2
P_{atm}	Atmospheric pressure, Newtons/m^2
P_{sat}	Vapor pressure of water at temperature T_{pn}, Newtons/m^2
Pr	Prandtl number
q_c	Convective heat flux, W/m^2
q_r	Radiation heat flux, W/m^2
R	Universal gas constant
$\dot{R}_i$	Volumetric chemical reaction rate for specie i appearing in r^{th} reaction, Kgmole/m^3sec
R_i	Net chemical reaction rate for specie i, Kg/m^3sec
Re	Reynolds number for gas flow
Re_{pn}	Droplet Reynolds number
r	Radial coordinate, m
S_m	Gas-liquid coupling term for mass
S_h	Gas-liquid coupling term for energy
S_i	Gas-liquid coupling term foe specie i
S^0_i	Standard entropy of formation of specie i
Sc	Schmidt number
Sh	Sherwood number for droplet
T	Temperature, K

T_{pn}	Droplet temperature, K
T_b	Boiling point temperature of water
T_{vap}	Minimum water vaporization temperature set at 287 K
T_{ref}	Reference temperature, 298.15 K
t	Time, sec
u	Gas velocity vector, m/sec
u_{pn}	Droplet velocity vector, m/sec
X_w	Mass fraction of water in air
X^0_w	Mass fraction of water in inlet air
x	Axial coordinate, m
Y_i	Mass fraction of gas specie i

Greek Symbols

β_r	Temperature exponent in Arrhenius rate expression for forward reaction r
$\eta'_{j,r}$	Concentration exponent in Arrhenius rate expression
ε_{pn}	Droplet emissivity
ξ	Radiation parameter, m
τ	Stress tensor, Newtons/m^2
λ_i	Thermal conductivity of specie i, J/m.sec.K
λ_m	Thermal conductivity of gas mixture, J/m.sec.K
μ_i	Dynamic viscosity of specie i, Kg/m-sec
μ_m	Dynamic viscosity of gas mixture, Kg/m-sec
$\upsilon'_{i,r}$	Stoichiometric coefficients for specie i in reaction r
$\gamma_{i,r}$	Third body efficiencies for specie i in reaction r
ρ	gas density, Kg/m^3
ρ_p	liquid water density, Kg/m^3
ϕ_{ij}	Dimensionless mixture property in the expression for mixture viscosity, μ_m
$\Omega_{\mu,j}$	Collision integral for gas viscosity
$\Omega_{D,j}$	Collision integral for specie diffusion
σ_p	Radiation scattering factor for droplet phase

Extinction Dynamics of a Co-flow Diffusion Flame by Very Small Water Droplets Injected into the Air Stream

1.0 INTRODUCTION

Development of water mist technology has been driven by the need to replace halogen-based, Halon 1301, fire-fighting agent. Halon 1301 affects the earth's ozone layer adversely, therefore it is banned from further production. Halon 1301 is a gaseous agent that can readily diffuse and interact chemically with combustion process by shutting off chain-branching reactions that are critical to the propagation of combustion. Water interacts with the combustion process mainly by physical mechanisms [1]. It is a multi-phase agent, whose transport, distribution, and evaporation impose challenges that necessitate considerable research efforts. In this paper, we present transient, axi-symmetric, computations on the effects of monodispersed, extremely small diameter (4 to 32 μm), water droplets on a co-flow, diffusion flame formed between two concentric cylindrical jets of propane gas (inner jet) and air (outer jet).

Typically, water mist is generated by forcing water through high-pressure spray nozzles and mist droplets have diameters between 50 and 200 μm. Sprinkler systems on the other hand produce droplets in the range of 1000 μm [2] while water hose systems produce much larger droplets. Most previous fire suppression studies [2-4] with water droplets have considered droplets from sprinklers and high pressure spray nozzles [5-6]. Ndubizu et al. [7] conducted experimental studies of water mist suppression of co-flow, methane diffusion flames formed in a slot burner (Wolfhard-Parker burner) and for pool fires [8]. They used high-pressure nozzles to form mists with Sauter mean diameter (SMD) of 30 to 66 μm. They showed that the flame temperature is reduced significantly at 7% mass fraction of water (SMD 66 μm) in the inlet air used for co-flow. Prasad et al. [9] modeled the experiments of Ndubizu et al. [7] by solving full Navier-Stokes (NS) equations, and using Eulerian-Eulerian sectional approach. The model predicted that the extinction concentration increases monotonically from 17.5 to more than 50% by mass as the drop size is increased from 50 to 150 μm. Recently, Liao et al. [10] developed a simple model (computationally fast) for water mist suppression of a co-flow diffusion flame by using boundary layer approximations to the NS equations. The U.S. Navy has developed fixed, total flooding, water mist technology for extinguishing fires in the machinery space of a ship using single-fluid, high momentum, high pressure spray nozzles [5]. Water mist and other total flooding agents are being developed for other parts of the ship including electronic spaces, flammable liquid storage areas, magazine protection, and other highly obstructed spaces.

Ultra fine mist (UFM) consists of extremely small water droplets, which are formed at atmospheric pressure using ultrasound vibration of piezoelectric discs similar to that used in commercial humidifiers. Recently, technology has been developed for extracting large throughput of ultra fine mist generated from the piezoelectric discs [11]. A significant number of studies are available on the fire suppression effectiveness of high-pressure nozzle mist [12,

13]. Relatively little is understood especially regarding the suppression and extinction of fires using UFM.

UFM droplets can follow the fluid flow streamlines and reach behind obstructions [14, 15] due to very small inertia. They do not wet surfaces significantly and may cause only a minimal damage to electronics [16] due to significant evaporation in dry air even at ambient temperature. Furthermore, UFM droplets have large settling times due to very low gravity effects. Therefore, a high concentration of the droplets may be suspended in air compared to the traditional water mist formed by the high pressure nozzles. Also, extremely small size droplets 1 to 10 µm can scatter and absorb the thermal radiation from a fire most effectively according to Ravigururajan et al. [17] when the droplet radius equals the wavelength of the thermal radiation.

Very few studies of diffusion-flame extinction with UFM are available in the literature. Ndubizu et al. [18-20] conducted experiments on the effects of UFM on a forced convection boundary layer flame formed over a burning polymethyl-methacrylate (PMMA) plate. They measured droplet distribution curves (volume frequency % vs diameter), which show a peak at 6 µm, SMD in the rage of 3 µm, and 90% (by volume) of the droplets have sizes below 20 µm. The water droplets are injected into the air flow over the burning plate. Ndubizu et al. [18-20] showed that, at a fixed inlet air velocity, the flame detaches from the leading edge of the plate and blows off as the UFM mass fraction is increased to a critical value (extinction concentration). The extinction water mass fraction was shown to decrease linearly from 7 to 1.5% as the inlet air velocity is increased from 60 to 120 cm/sec. Ananth et al. [21, 22] modeled the PMMA experiments of Ndubizu et al. [18-20] and obtained computational solutions of the time dependent Navier-Stokes equations for the extinction of the PMMA boundary layer flame due to the injection of monodispersed water droplets. They used an Eulerian-Eulerian sectional approach to model the droplet dynamics and showed that the degree of droplet evaporation near the leading edge of the flame plays a key role in extinguishing the flame. The computations show that the reaction kernel detaches from the leading edge of the plate and the flame blows-off at or above the extinction concentration. They used single step chemistry and showed that the maximum heat release rate (or reaction rates) decreases significantly at extinction. It is generally known [23] that flame blow-off occurs when the maximum Damkholer number (Da) or maximum heat release rate fall below a critical value. Ananth et al. [22] predicted that the extinction mass fraction of water decreases from 9.5 to 1.8% as the air velocity is increased from 60 to 170 cm/sec for 6 µm drops. The calculations of Ananth et al. [22] exhibit a minimum in extinction concentration as the drop diameter is increased from 6 to 100 µm. At a fixed air velocity of 84 cm/sec, the water extinction concentration decreases from 9.5 to 5.5 mass % as the drop size is increased from 6 to 40 µm. A further increase (40 to 100 µm) in the drop diameter increases the extinction concentration from 5.5 to 13.5 mass %. The computations show clearly that large drops are more effective than small drops in the range between 6 and 40 µm, and the converse is true at drop sizes above 40 µm. As the air velocity is increased to 170 cm/sec, the computations show that the extinction concentration is less dependent on the drop size. Lentati and Chelliah [24, 25] modeled extinction of one-dimensional, counter-flow, diffusion flames by water droplets, and showed that the physical effects dominate over any chemical effects. In the counter-flow geometry, large jet velocities of air and methane (order of 2 m/sec) are employed.

They showed that the extinction strain rate is lowered with the addition of water to the air stream, and the physical effects dominate over any chemical effects. Using a Lagarangian approach, they calculated the droplet trajectories and a non-monotonic relationship between extinction strain rate and drop size (5-50 μm). Their calculations show a minimum in the extinction strain rate with increased drop size from 5 to 50 μm. Zegers et al. [26] performed experiments on the monodispersed water droplets' extinction of counter-flow, propane, diffusion flames. They showed that the extinction concentration remained constant between 14 and 30 μm and then increased with increasing drop size between 30 and 42 μm.

Recently, Fisher et al. [27] performed experiments on UFM (polydispersed, D_{10}=6.2 μm) extinction of a co-flow, diffusion flame formed between two concentric jets of air and propane, similar to the geometry considered in the current paper. They performed flow particle imaging velocimetry and flame imaging to show that the water drops evaporate well outside the flame, and the water vapor is entrained at the base of the flame. As the water concentration is increased, the flame base lifts up from the burner and blows-off at extinction. Fisher et al. [27] reported that the flame extinguished at 12.5% mass of water drops (D_{10}=6.2 μm) in inlet air, which is saturated with water vapor (1.4 mass %). The co-flow geometry and the flow rates of air and propane considered in the experiments of Fisher et al. [27] are similar to those considered in the recent computational work of Ananth et al. [28]. Ananth et al. [28] showed that 4 μm monodispersed droplets evaporate at the 100 ^{0}C isotherm, which is well outside the reaction zone of the flame. They also showed that the predicted extinction concentration for 6 μm drops is in excellent agreement with that measured in the experiments of Fisher et al. [27]. Shilling et al. [29] conducted experiments on the ultra fine water mist (8.2 μm volume median diameter) extinction of heptane pool flame formed in a cup-burner. They measured that about 14.5 mass % water is needed to extinguish the flame. Adiga et al. [15] conducted computational and experimental studies of UFM extinction of a 120 KW heptane pool fire inside a 28 m^3 compartment. The experiments show about 9 mass% water is needed to extinguish the fire in 5 minutes. The extinguishment time decreased with increased concentration of water in the compartment.

In the current paper, we consider an axi-symmetric diffusion flame formed between two concentric cylindrical jets of air and propane. After a stable flame is established, a suppression agent (nitrogen or mono-dispersed droplets) is injected into the outer air jet at the bottom of the burner at a fixed mass fraction. We obtain numerical solutions of the laminar, transient, Navier-Stokes and energy equations for the gas phase and the Lagrangian form of the droplet conservation equations using finite-volume techniques with the CFD software package Fluent in cylindrical geometry as described by Ananth et al. [28]. In the case of nitrogen, the specific heat and latent heat effects are absent, and the flame extinction occurs due to oxygen dilution as the nitrogen concentration in the co-flow air is increased to a critical value. The predicted extinction concentration is in excellent agreement with the recent measurements reported by Linteris et al. [30]. In the case of water injection with the co-flow air, the droplets' trajectories are calculated from the injection point and into the flame. The droplets travel up against gravity, and entrain into the flame. As the droplets approach the flame, they evaporate, absorbing energy equal to the latent heat of vaporization, to form water vapor. Water vapor absorbs additional energy as

the sensible heat due to its higher (two times) heat capacity than that of the air. These processes lead to cooling at the flame and subsequent reduction in the combustion reaction rate due to the lower temperature. The water vapor also dilutes the oxygen in the air and directly reduces the combustion reaction rate and heat generation. Ultimately, flame extinction occurs when the heat generation rate is not sufficient to heat the flow of fuel, air, and water (by convection and diffusion) to the flame temperature. For fixed air and fuel gas flow rates into the burner, there exists a critical combustion rate or critical Damkholer number (Da) below which the flame blows off from the edge of the inner fuel tube and extinguishes. This is similar to the blow-off phenomena described by Chen and Tien [23] near the leading edge of a boundary layer flame. We choose a chain-branching reaction as an indicator to follow the extinction process caused by the cooling and dilution effects of water. The chain-branching reaction rate is maximum at the flame base and is shown to decrease below a critical value, as the injected droplet mass fraction was increased above a critical value, until flame extinguishment occurred. The droplet size was varied from 4 to 32 μm to study its effect on the extinction droplet concentration. The predicted extinction concentrations of water for 4 and 8 μm sizes are consistent with the experimental measurements of Fisher et al. [27] for 6.2 μm average size (D_{10}) drops.

The evaporation rate increases as the inverse of the square of the diameter (d^2 – law) for fixed mass concentration of water. Therefore, an order of magnitude decrease in drop size nominally should lead to two orders of magnitude increase in the evaporation rate for UFM compared to that for spray nozzle mist. However, combustion occurs within a narrow band of equivalence ratio within the core region of the flame, where fresh fuel gas and air come in contact. Therefore, the heat generation rates are inhomogeneous. This means that the dynamics of droplet evaporation (the location and the rate of evaporation) will have a critical, but not yet completely understood, role in determining whether extinction occurs in diffusion flames. For example, extremely small water droplets might evaporate before reaching the flame region containing the maximum heat generation rates. Extinction would not occur because of the gap between the region of evaporation and the region of high heat generation. On the other hand, relatively large droplets might penetrate the core of the flame but may have evaporation rates that are too low for flame extinguishment. The minimum value of the mass fraction (extinction concentration) of the droplets in air needed to extinguish a flame is not known. The effect of droplet size on the extinction concentration is also not well understood. Increasing the droplet size increases inertia and may inhibit entrainment into the core of the flame as well as reducing the evaporation rate. All of these issues can have critical implications in highly obstructed areas such as the electronic and machinery spaces of a ship.

2.0   THEORETICAL

The burner consists of two concentric tubes with diameters 2.5 cm and 10 cm as shown in Figure 1. Propane is injected into the inner tube and dry air is injected into the annular region respectively. As the propane emerges from the inner tube, it mixes with the air stream. Upon ignition, a diffusion flame is formed just above the rim of the inner tube. As the gases get hot, they accelerate and drag the surrounding air into the flame. The flow of hot gases influences the flow of air below the rim of the inner tube. Therefore, we include an entrance region of 3 cm

length below the rim of the inner tube in the model to account for the effects of the flame-generated fluid dynamics on the injected air streamlines. This includes the effects of the boundary-layer formation on the side walls of the entrance region, where the droplets travel slower than in the bulk.

Figure 1 shows a sketch of 1900 and 373 K temperature isotherms of the flame. The region between the two isotherms is the thermal boundary layer (pre-heat zone). Figure 1 also shows the flame base, the region where the flame "attaches" to the edge of the fuel tube. In the diffusion flame, heat is released along the entire length of the flame as mixing occurs between oxygen in the air and the intermediate species generated by combustion. Fresh oxygen meets fresh fuel at the base of the flame, where the combustion rate is the highest. Figure 1 shows the reaction kernel, which is defined as the region surrounding the location of the maximum reaction rate within the flame base. The reaction rate falls steeply (by an order of magnitude) outside the reaction kernel. The thermal boundary layer extends well beyond the reaction kernel and the droplets must penetrate the thermal boundary to reach into the reaction kernel. This point will be investigated in detail later in the paper during the discussion of extinction phenomena.

In addition to diffusion, the buoyancy-driven flow due to high temperature gradients affects the degree of entrainment of air into the flame and the associated mixing among species. The Grashof number, Gr, is of the order of $2x10^8$ based on an average temperature of 1500 K and the diameter of the outer tube. This is much bigger than the square of the injected air Reynolds number of 4×10^5 (Re=650). This suggests that the bulk of the air is affected by the natural convection and deviates significantly from the streamlines of the injected air at the bottom of the burner. Therefore, the fluid flow set up by the natural convection is intrinsically transient as vortices form and rise up the chimney as sketched in Figure 1. The buoyancy effects on the flame base are relatively small. Near extinction, the flame base becomes highly transient primarily due to the introduction of water droplets.

Very little theoretical work can be found in the literature for co-flow, propane, diffusion flames formed in an axi-symmetric geometry even in the absence of water droplets. A full description of the chemistry for propane combustion involves over 400 reactions and 80 species, and requires very high computational power. Computationally efficient (reduced), propane chemical mechanisms that are validated by experiments are not available in the literature for the present geometry. In this paper, we do not intend to conduct a study of the chemical mechanisms. Instead, a reduced mechanism consisting of 35 species and 217 reactions is used to
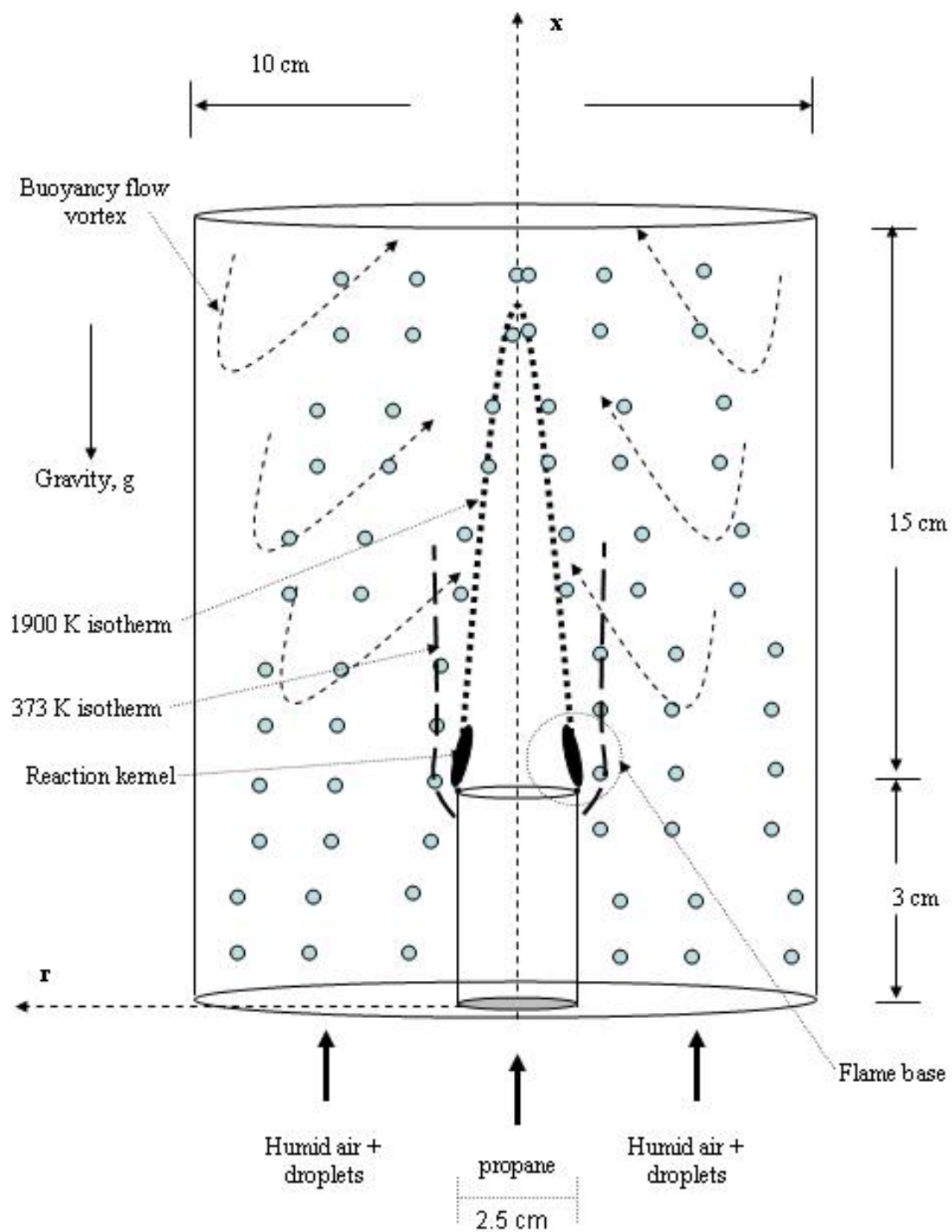
Figure 1.   Computational model for the interaction of ultra fine droplets with an axisymmetric co-flow diffusion flame

describe the combustion chemistry. This is the same as GRI 3.0 (Gas Research Institute, *http://www.me.berkeley.edu/gri_mech*) mechanism except the nitrogen containing species (N_2 is included) are neglected. GRI 3.0 is used widely in literature for methane combustion containing a small fraction of propane. It does not include all of the propane pyrolysis products. Specifically, it does not contain C_3H_6, C_3H_5, C_3H_4, and C_3H_3 which are included in the San Diego propane mechanism, which was studied by Cheng et al. [31] for premixed, counter-flow geometry. However, GRI 3.0 includes all of the oxidation chemistry and the formation of the pyrolysis product C_3H_7. As discussed later in the present paper, we also performed computations for nitrogen as the extinguishment agent instead of the water droplets. The computations predict the extinction concentration of nitrogen within 10 % of the experimental measurements reported recently by Linteris et al. [30] in a cup-burner. The cup-burner experiments of Linteris et al. [30] also show that the nitrogen extinction concentration is 23 % lower for methane flame than for propane flame. Therefore, the use of GRI 3.0 in place of full propane chemistry in our Navier-Stokes model may cause less than 10 to 23 % error in the extinction concentrations for a physical agent such as nitrogen.

A system of two-dimensional, transient, Navier-Stokes and energy equations are solved in cylindrical geometry (x,r), where x and r are axial and radial distances as shown in Figure 1. We assume axial symmetry and the transport in φ direction are neglected. The equations for laminar combustion in the gas phase are given in Appendix A by equations (A1-A39). They include pressure-velocity coupling, gravity term in the x-direction, Dufour effects, gas radiation effects without soot, and the GRI 3.0 combustion reaction chemistry. Gas density depends on temperature according to the ideal gas law. The diffusive fluxes are written based on ideal gas mixture properties, which are evaluated using Chapman-Enskog equations. The transport and thermodynamic parameters provided in the GRI 3.0 database are used for individual species. Radiative transport does not play a crucial role in the extinction because of the small size (1.25 cm) of the flame. However, a gray-body radiation loss from the flame to the surroundings is included using a simple P-1 radiation model for the gas medium. A separate gray gas radiation equation (P-1 model) is solved and radiative flux from hot gases is computed to include in the energy equation as shown in the Appendix. Soot formation is neglected because it is expected to be small near the base of the flame, where the extinction phenomena occur. Soot concentration is expected to increase downstream, and is not considered in the computations of flame extinction. A set of ordinary differential equations describe the species consumption and production rates, R_i, due to the chemical reactions alone. Arrhenius reaction rates are evaluated using the chemical database of GRI 3.0.

Even though water mist extinguishes the flame mainly by physical mechanisms rather than chemical, it is convenient to follow the extinction phenomena in time by following the progress of a chain branching reaction rate. The GRI3.0. mechanism contains the following chain branching reactions:

$$O+H_2=OH+H \qquad\qquad (1)$$

$$O_2+H=OH+O \qquad\qquad (2)$$

The computations showed that both the reaction rates have very similar contours. They both peak at the base of the flame forming a reaction kernel, which is the region of high rate of reaction. We will show that the maximum rate of reaction (1) inside the kernel decreases dramatically with time during the extinction process for different values of droplet concentrations and sizes, therefore, reaction (1) is a reasonable indicator of the progress towards extinction. Since chain-branching is an essential process of combustion, a decrease in chain-branching rate signifies a decrease in the combustion rate and the associated Damkholer number, Da. We will show that reaction (1) provides a simple, coherent, interpretation of the complex computations of the extinction phenomena. It is likely that other choices of the reaction steps may also help explain the computational results.

Inlet velocity and composition are fixed. At the outlet, the pressure is set to be atmospheric. This allows for both inflow and outflow of gas at the top of the outer tube. No slip is prescribed on all the burner walls. The top edge of the inner tube gets hot due to the heat transfer from the flame, which stabilizes at the rim of the inner tube. The heat loss to the inner tube is included in the model by assuming that the tube wall is at 600 K for a length of 1 mm below the top edge. The rest of the inner tube wall and the entire outer tube wall are set at ambient temperature. The fuel flow velocity, temperature, and composition at the edge of the inner tube are also specified. In the cup-burner experiments [27, 30], the fuel gas passes through a bed of glass beads, which are exposed to the flame. Measurements of fuel temperature, composition, and velocity at the exit of the inner tube are not yet available. However, Ndubizu et al. [7] measured a fuel temperature of about 623 K at the exit of a slot burner filled with sand. This is because of heat feed back upstream by conduction and radiation from the flame to the sand particles at low fuel velocities, which are typically encountered in co-flow burners. Therefore, we imposed 600 K boundary condition for the fuel emerging from the inner tube in the current computations. We also imposed 2 cm/sec velocity for the fuel flow from the tube so that it is equivalent to 1 cm/sec velocity at STP conditions. Furthermore, we neglect back diffusion of species from the flame into the fuel tube despite the low fuel velocity, and assume that the fuel emerging from the tube is 100% propane consistent with earlier works [9, 30, 32].

The dynamics of each droplet from injection at the inlet to complete disappearance by vaporization or outflow is described by a set of ordinary differential equations, which are given in Appendix A by equations (A49-A60). They describe drop trajectories, mass, momentum, and energy balances for each droplet of water. The droplet is assumed to be spherical and the internal gradients of momentum and energy are neglected in view of extremely small size range considered in the computations. This assumption is typically used for water [9, 22, 24, 25, 28, 32]. Liquid water has five times higher thermal conductivity than a typical hydrocarbon liquid such as heptane. We estimate that the conduction time scale for internal droplet heat transfer $(d_p^2/4\alpha_l)$ is ten times smaller than the evaporation time scale for a 4 μm droplet. Here, d_p and α_l are the droplet diameter and thermal diffusivity of liquid water respectively. Therefore, the droplet is assumed to be at uniform temperature with no internal circulation. For extremely small droplets, thermophoretic force acts in the direction of decreasing temperature and can decelerate the droplet as it approaches the flame. However, at small drop size, the droplet evaporates very quickly before it is exposed to a significant temperature gradient. We estimate less than 2% deviation between droplet and gas velocities due to the thermophoretic effects for 4

μm diameter near the 600 K isotherm (2000K/cm gradient) at the base of the flame using the relationship given by Talbot et al. [33]. The Brownian and Saffman lift forces become significant only for submicron drops, therefore they are also neglected compared to the drag force.

We consider initial droplet sizes as small as 4 μm, which can only persist in saturated air at room temperature. Therefore, we assume that the injected air is 100% humid (or 1.8 % mass water vapor) when the droplets are present regardless of the size. After a base-case flame is established, we switch the air composition from dry air to a mixture of 100% humid air and droplets (inlet boundary condition). The mono-dispersed droplets have pre-specified mass fraction. As the mist travels up it pushes out the dry air that exists initially in the burner. At the mist front, some mixing occurs due to diffusion of water vapor from the mist region to the dry air and the local humidity drops below 100%. This causes droplets to evaporate at room temperature near the mist front for the case of very small drops. However, the evaporation rates are very small (10^{-9} kg/sec) compared to those inside the flame. In the bulk of the mist, the air remains saturated and droplets remain at the initial size until they reach the flame and interact with the hot gases. All the walls are set as reflective boundaries. The droplets in contact with the hot part (1 mm length) of the burner tube are set to evaporate completely.

Droplet evaporation rates play critical role in the flame extinction and are determined by the heat transfer rate to the drop surface. The conduction/convection heat transport to the spherical surface of the drop dominates over the radiation transport at small drop diameters (4 to 32 μm). Tseng and Viskanta [34] computed evaporation rates of a semi-transparent, single, droplet inside a combustion environment using a (spectral) band model. The model includes the three modes of heat transport as well as the mass transfer effects. Figure 12 of their paper shows that the radiation absorption from a gas at 1500 K has no effect on the lifetime of 10 μm drops. Inclusion of radiative heat transfer decreases the lifetime by about 40% for a 100 μm drop. Therefore, the radiation effects on the water droplets are neglected.

We will show that only a small portion of the mist entrains into the flame base, and the entrained droplets evaporate completely near the flame edges (600 K isotherm). Most of the mist travels vertically up the chimney. The evaporation rates of the bulk mist are not affected significantly by radiation from the flame because the mist is injected at 100% humidity, which minimizes the mass transfer driving force needed for evaporation. Recently, Tseng and Viskanta [35] modeled radiation absorption and scattering through a sheet of mist based on Mie scattering theory for semi-transparent, linearly anisotropic water drops. In their Figure 12, Tseng and Viskanta [35] showed decreased total absorptance and increased total transmittance of radiation from an external (black-body) energy source with increased surface droplet density (product of number density and sheet thickness). From their Figures 12 and 13, we estimate the absorptance and transmittance through 5 cm (outer tube radius) thick bulk mist to be 0.28 and 0.5 respectively near extinction water concentration (12 mass%) and 10 μm drop diameter. Therefore, the bulk mist contribution to the radiation loss from the flame base is neglected for the small, non-sooty, flame with low emissivity and steep gradients. However, in real applications for large-scale sooty fires, water mist contribution to radiation effects can be significant for large, poly-disperse droplets.

Solution of the droplet equations (A49-A60) gives droplet velocity components, temperature, and diameter as functions of time. Collision between drops are neglected at low liquid volume fraction (10^{-4}). Droplet fragmentation is neglected because of low values of Weber number (10^{-5}). The gas phase affects the droplet phase through equations (A49-A60), and the droplet phase affects the gas phase through the coupling terms, which appear as point sources/sinks in the gas phase equations (A1-A6). The coupling terms describe the exchange of mass, momentum, and energy between the gas and droplet phases, and are given by equations (A40-A48).

In equation (A40), S_m represents total mass (water vapor) exchange rate from the droplet phase into the gas phase due to evaporation. It depends on droplet size and concentration. This term affects the gas density and composition in the continuity (A1) and specie (water vapor) balance (A4) equations respectively. The water vapor is formed at $100\ ^0C$ and it is heated up to the local gas temperature. The water vapor has higher specific heat than the air. In addition to the sensible heat absorption, water vapor dilutes the species' concentrations given by equation (A4) and decreases the oxygen concentration available for the combustion reaction. The coupling term, F_d, represents the total drag exerted by the droplet phase on the gas phase, and is given by equation (A43). The term, S_h, represents the total cooling rate due to the water droplets, and is given by equation (A46). The total cooling rate includes the sensible heat absorption due to droplet heating and latent heat of evaporation. The second and third terms on the right hand side of energy equation (A3) represent the cooling rate, S_h, and the combustion heat release rate respectively, and have opposite signs. The heat release rate depends on the reaction rates, R_i, which decreases due to the oxygen dilution by water vapor according to equation (A13). The convective term on the left hand side of energy equation (A3) represents the energy needed to heat up the gas phase from ambient to the flame temperature. In equation (A3), the transient term will be negative, if the sum of convective and conductive heat loss and the cooling rate, S_h, is higher than the heat release rate. Therefore, the gas temperature decreases with time. A small decrease in gas temperature further reduces the heat release rate significantly due to the exponential nature of the Arrhenius equation given by (A14). Therefore, the flame will approach extinction. Indeed, Da represents the ratio of heat release rate and the heat loss rate by convection and conduction. As the flame approaches extinction, Da decreases. In the case of flame extinction using an inert gas (such as nitrogen addition), all the coupling terms (A40-A48) vanish unlike the mist case. The inert gas dilutes oxygen and specie concentrations in equation (A13), and reduces the reaction rate, R_i. Therefore, the inert gas addition reduces the heat release rate, the second term on the right hand side of energy equation (A3). This drives the competition between the sum of convective and conductive heat loss, and the heat release rate in equation (A3) towards flame extinction by decreasing Da below its critical value.

3.0   NUMERICAL

The gas-phase differential equations are discretized using the finite-volume method over a mesh consisting of 100 x 220 tetrahedral cells. The smallest cells (0.2 mm x 0.3 mm) are placed in the flame base region near the rim of the fuel tube. The cell size increases with increasing values of x and r from the inner tube rim. The finite-volume equations are solved using implicit numerical schemes available in Fluent including a stiff chemistry solver. The gas-phase equations are solved using a segregated solver with second-order upwind method. A SIMPLE family of schemes (PISO) is used for the pressure-velocity coupling. Ignition is achieved by raising a region above the fuel tube to a high temperature for a very short time relative to the simulation time.

The droplets are injected at a pre-specified (constant) flux at the air inlet so that the mass fraction of water in the inlet air is fixed. The inlet flow of water is divided into a number of injection tracks (1 injection/cell) along the inlet.   For extremely small drops (4 μm), it is too expensive to solve the Lagrangian droplet equations for every droplet since there are a few millions of drops. Therefore, the equations are usually solved for a representative drop for every few hundred drops injected. At a given time, the solutions obtained for the representative drop are scaled by a factor of few hundreds in a given injection track to calculate the coupling terms (A40-A48) for the entire mass of water. As the drop size increases, the number of drops decreases significantly so that the droplet equations are solved for every droplet. Lagrangian droplet equations are solved using implicit schemes available in Fluent. Full coupling between the gas phase and droplet phase is achieved by updating the droplet source terms every time the gas-phase equations are iterated. The gas-phase equations are iterated ten times per iteration of the droplet phase.   The time steps are 50-100 μsec for the gas phase and 1-5 msec for the droplet tracking.

The residuals are reduced to 0.1% for convergence. The residual for the gas phase energy equation is reduced to 10^{-4} %. In a typical computation, the residual of the continuity equation decreases the slowest with the number of iterations, and controls the convergence. The calculations are computationally intense and are performed on SGI Altix 3700 parallel machine (13.1 peak TeraFLOPS) through DOD High Performance Computational resources. It consists of 2048 Intel Itanium 2 (1.6 GHz each) processors. A typical CPU time is 18 hours for 2000 time steps using 36 processors with a run time of 28 hours. A typical run requires 25000 time steps.

4.0   RESULTS AND DISCUSSION

First, we modeled the flame without any suppressant to establish the base case. The left half of Figure 2 shows the streamlines and the temperature contours at time=5.39 sec. The streamlines show clearly that the entire flow in the tube is affected by the presence of the flame. They extend far beyond the thermal contours. The flame is attached to the edges of the fuel tube exit, where fresh air mixes with the fresh fuel and the reactions occur rapidly releasing heat. As the gas temperature increases, the gases expand and accelerate towards the top of the burner at velocities as large as 3 m/sec. As they accelerate, they drag air into the flame as indicated by the
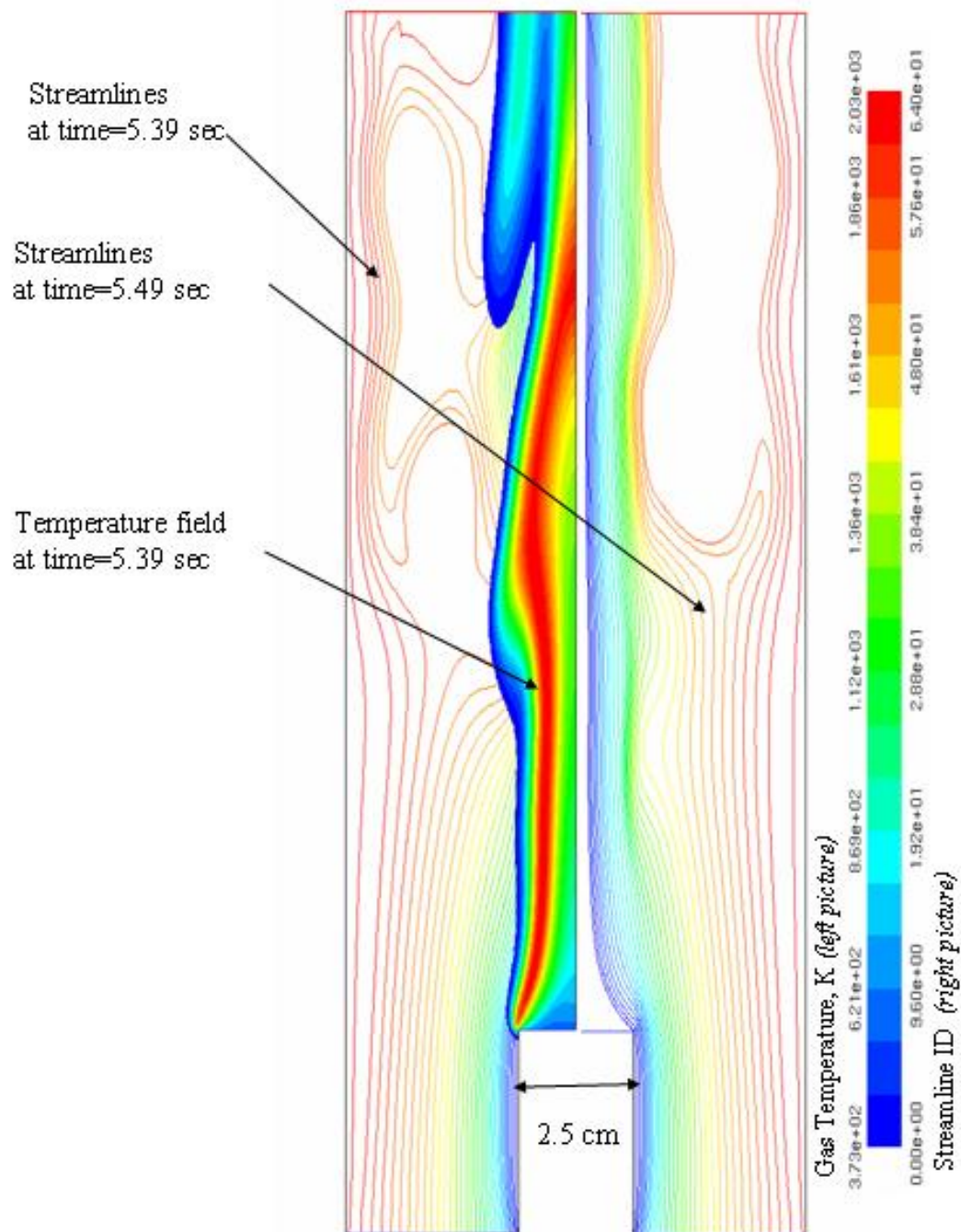
Figure 2.   Time dependent flow and temperature fields without the water mist
             Left half of the burner: Streamlines superimposed on temperature contours
             without mist at 5.39 sec
             Right half of the burner: Streamlines without mist at 5.49 sec

streamlines that are bent towards the flame. The flame temperature increases with x to about 2000 K and decreases slowly as it approaches the chimney exit. The large temperature gradients in the radial direction cause buoyancy-driven flow, which increases with the distance, x, from the fuel burner tube. The left half of Figure 2 shows the formation of two vortices in the bulk air. These vortices begin to form at some vertical distance (about 2 times the diameter of the inner tube) from the rim of the inner tube. The vortices grow in size as they slowly travel upward in x-direction. The right half of Figure 2 shows the streamlines of the injected air at 0.1 sec later (time=5.49 sec). The two vortices merged into one. As the vortex travels further and exits at the top of the chimney, it entrains air/combustion products from outside into the chimney. The entire process repeats itself with time. The vortices cause flickering, which is especially evident at large values of x. The flickering effects are much more pronounced in short, puffing, diffusion-flame formed over a liquid pool surface, which exhibits flow instabilities caused by the heat feed back [32].

Figure 3 shows the radial temperature profile at 10 mm (x=4 cm) above the burner. The temperature increases with the radial distance and reaches a maximum (about 2000 K) at the reaction kernel and decreases to ambient temperature in the bulk air. Clearly, the gradient is much steeper on the air side than on the fuel side. The gas temperature reaches the boiling point for water (373 K) at about 5 mm radial distance from the peak. Figure 3 also shows the concentration (mole fraction) distributions for OH, H, O, CH_3, and C_2H_6. Clearly, the OH, H, O radicals are formed in the reaction kernel located around r=1.0 cm from the axis of symmetry. The thermal boundary layer extend much farther than the reaction core as indicated by the temperature profile, which reaches ambient temperature at r=1.5 cm. Clearly, any droplet traveling towards the flame must survive the thermal barrier to reach into the reaction kernel. The temperature and specie profiles also change with the axial distance, x. As the axial distance increases, the core of the fuel gets hot and the peak temperature position moves towards the axis of symmetry. Our computations showed that the flame length is about 15 cm as indicated by the value of x (x=18 cm), where the temperature peak occurs at the axis of symmetry.
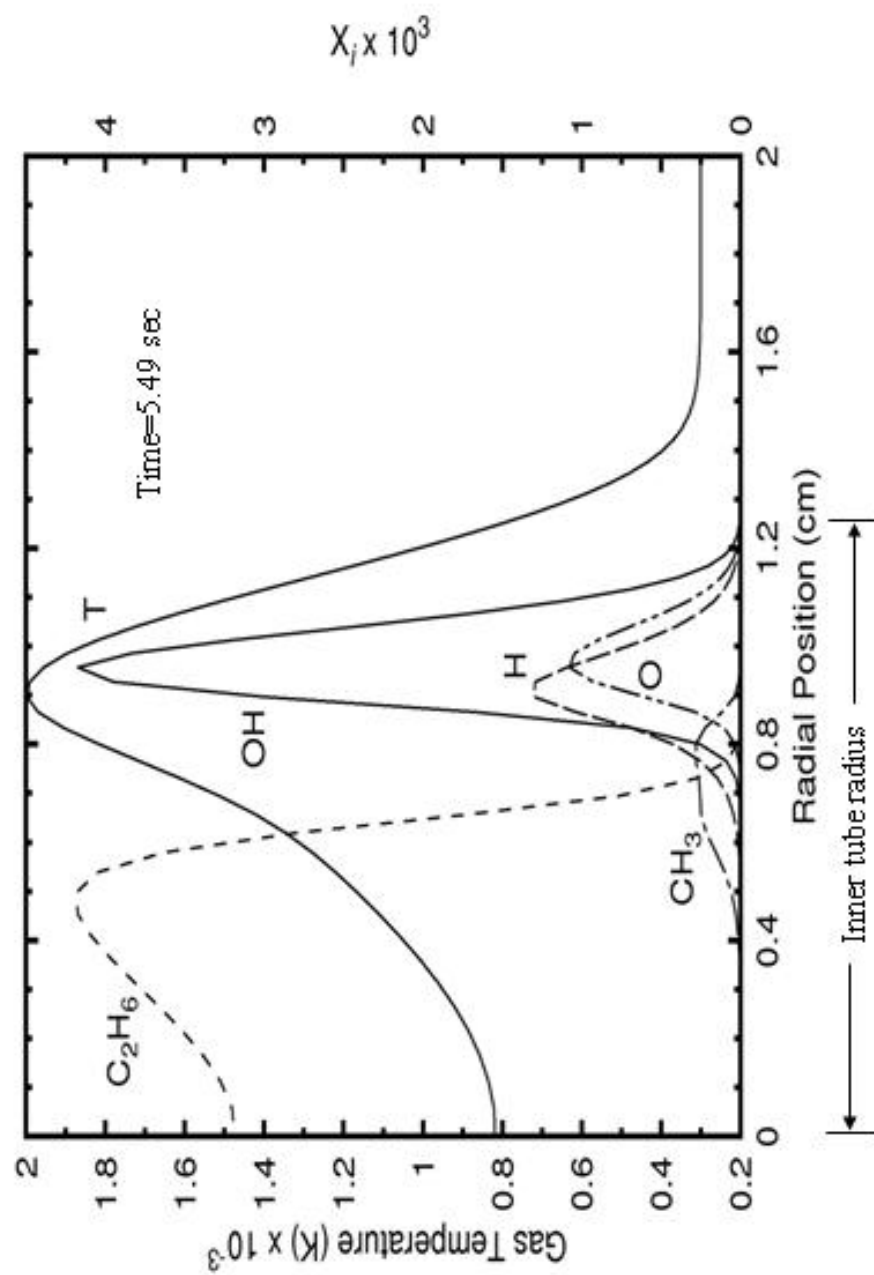
Figure 3.   Radial distributions of temperature and species mole fractions 1 cm above the burner rim without water mist

We are not aware of earlier work on co-flow, propane, diffusion flame simulations. The present computations provide the detailed thermal and chemical structure of the flame. However, in the present paper, we focus on the extinction phenomena rather than a detailed presentation of the base case without the mist. Figure 2 clearly shows that the structure of the flame is time dependent due to the buoyancy effects, which cause flickering. However, the flow near the flame base region (within one radius height from the inner tube exit) is relatively smooth. The co-flow air stabilizes the flame base by pushing the vortex formation downstream. A small degree of oscillations at the flame base persist and cause the maximum flame temperature to fluctuate slightly with time. When we introduce droplets, the droplets also can cause fluctuations due to their discreet nature at small droplet concentrations by volume. More importantly, the droplets cause dramatic changes in the flame position with time. Our computations are time dependent, and therefore include both the primary temporal effects due to droplets and the secondary temporal effects due to buoyancy flow on the extinction of the flame. In the interpretation and discussion of the computational results, however, we focus on the primary mechanisms of flame extinction dynamics caused by the water droplets, and leave the discussion of the two-dimensional oscillatory effects for a future time. In the present paper, we will show that the degree of droplet entrainment and evaporation in the flame base region plays a critical role in flame extinguishment.

First, we introduced nitrogen into the co-flow air. Computations were performed at different values of the nitrogen mass concentrations at the air inlet. As the nitrogen concentration reaches a critical value (extinction concentration), the flame base detaches from the inner tube and travels downstream (blows-off). Our computations predict the nitrogen extinction concentration to be 36 mass %. Recently, Linteris et al. [30] reported the nitrogen extinction concentration for propane cup-burner flame to be 33.3 mass %. In the cup-burner experiments, the measurements of temperature, velocity, composition of the fuel gas at the inner tube exit were not reported. As discussed in the theory section, the conditions at the inner tube exit are not well defined because they are coupled to the flame downstream. This is due to the back diffusion (and radiation) of heat and mass from the flame to the inner tube exit upstream, and idealizations are made in theoretical models to decouple the boundary [9, 32]. Therefore, small differences may exist between the actual conditions and the idealized boundary conditions employed in the present computations at the inner tube exit. This idealization and the use of GRI 3.0 mechanism may be responsible for about 10 % deviation between our predictions and the measured values for the nitrogen extinction concentrations. Linteris et al. [30] also reported nitrogen extinction concentrations for ethane and methane flames in the cup-burner to be 35.3 and 26.5 mass % respectively. Their experiments show that the extinction concentration is insensitive to the air flow velocity. Sheinson et al. [36] performed cup-burner experiments on the extinction of diffusion flames formed over n-heptane liquid pool by different diluents, including nitrogen, introduced into the air co-flow of about 4 cm/sec. They reported 29.4 mass % (within 3% accuracy) nitrogen in the air feed is needed to extinguish both n-heptane and 2-propanol liquid pool flames. The liquid pools may have significantly different surface temperatures than the temperature of a gaseous jet at the exit of the inner tube. Based on the cup-burner experimental results for gases and liquid pools, with the possible exception of methane, the nitrogen extinction concentration appears to be insensitive to the conditions (velocity, temperature) at the exit of the inner tube boundary, and the chemical nature (chain

length) of the hydrocarbon fuel. It may not be surprising that the details of chemical mechanisms do *not* play a critical role in co-flow diffusion flames unlike in premixed flames for physical suppression agents. This is likely because transport effects dominate in co-flow flames and chemical effects become significant only very close to the extinction point. Even in counter-flow diffusion flames, where the flame is highly stretched and the flame is close to extinction to begin with, the chemical effects are found to be insignificant [24, 25].

Flame extinction can be viewed as a blow-off (or blow-out) phenomenon that occurs when the heat generation rate due to the combustion reactions is insufficient to heat the fuel and air supply to the reaction front, and Da reduces below a critical value [37], as explained at the end of the theory section. The air and fuel supply to the reaction front occurs by convection and molecular diffusion. The reaction front lies in a region, where the oxygen and fuel are within the flammability limits. In the absence of an extinction agent, the intrinsic reaction rates are very high, and the air/fuel supply rates control the location of the reaction front. If the fuel flow rate is increased significantly to overwhelm the heat generation, the flame front moves downstream, and eventually blows off as Da decreases below a critical value [23]. Similarly, addition of an inert gas (e.g., nitrogen) to air reduces the heat generation rate due to oxygen dilution. Our simulations show that the flame front moves away from the burner rim and blows off as the mass fraction of nitrogen is increased to a critical concentration of 36% with the fuel flow rate fixed. If instead of nitrogen, a gas with higher specific heat than air is added, a different effect comes into play. Water vapor has twice the specific heat of air. Therefore, water vapor absorbs more energy as sensible heat from the flame front and reduces its temperature, in addition to the dilution effect. This cannot be easily observed in practice due to condensation of vapor above the saturation limit. To quantify the specific heat effect, computer simulations are performed with high mass fractions of vapor without letting condensation occur. The simulations show flame extinction by blow-off at water vapor mass fractions of 17 to 20 %. The oxygen dilution and specific heat effects are coupled and nonlinear. This is because both lead to a decrease in flame temperature, which decreases the rate of critical temperature-dependent reactions and the heat generation rate. At that point, changes in flame position accelerate, the flame becomes unstable, and eventually is extinguished. The two effects are separate and distinct, and are determined by two independent parameters: mass fraction and specific heat of the extinction agent.

Evaporation of water drops includes three effects: oxygen dilution, latent heat absorption, and extra sensible heat absorption due to the higher specific heat of water vapor than air [7, 9]. Therefore, the evaporation rate plays a key role that is absent for gaseous extinction agents. The evaporation rate depends on droplet concentration and size. This introduces droplet size at the injection plane as the additional independent parameter. Furthermore, the droplet supply rate (or entrainment) to the flame front depends on inertia, drag, and gravity. The droplet dynamics introduces other independent parameters: the droplet-velocity-vector components at the injection plane. In our simulations, after the base flame is established, we inject a mixture of mono-disperse droplets and water vapor at the air inlet, at a velocity identical to that of air. The water vapor is equivalent to 100 % humidity (1.8 % by mass) at ambient conditions. We vary the droplet concentration to determine the point of flame extinction for a fixed droplet size. We also determine the effects of droplet size on the extinction mass fraction of water droplets.

Next, we discuss the computations for 8 μm water droplets. The droplets are introduced at a fixed concentration of 10.2 % (+1.8 % vapor, 100 % humidity) by mass. Figure 4a shows the droplets at 0.34 sec (time=5.34 sec) after we begin to inject the water. The left half of Figure 4a shows the droplet trajectories, which are color coded by their injection position along the air inlet. The blue solid circles represent droplet tracks injected close to the wall of the fuel tube and the red circles are droplet tracks injected farther from the wall. Figure 4a shows the two dimensional view of the axi-symmetric water injections. Therefore, each droplet track represents a concentric circles around the flame. Also shown in Figure 4a are the streamlines (solid lines) of air, which are also color-coded like the droplet injections. The droplets appear to follow the streamlines closely due to large surface-area-to-volume ratio. The droplets and air adjacent to the wall travel at a significantly slower velocity than those away from the wall due to the no-slip condition imposed at the wall. Therefore, the droplets (blue) adjacent to the wall have not reached the flame base region at the rim of the burner (inner tube) yet as shown in Figure 4a. Indeed, the droplets take 0.6 sec from the time of injection to reach the flame base region.

We show the chain-branch reaction ($H_2+O=OH+H$) rate contours in color in Figure 4a. The colors correspond to the magnitudes of the reaction rate, which are shown on the left side of the vertical bar. The red color region at the flame base represents the reaction kernel, region of high reactivity. The peak reaction rate occurs within this kernel. The reaction rate decreases with the axial distance as the products are formed, and the reactants get diluted. Figure 4a also shows the 373 K isotherm, which is shown as a solid green line that cuts through the air streamlines. It shows that the thermal gradients extend a millimeter or less near the flame base into the air side and the droplets are about to reach the boiling-point temperature isotherm (for reference, the radius of the inner tube is 12.5 mm in Figure 4a). The right half of Figure 4a also shows the same chain-branching reaction rate contours (colors correspond to the magnitudes shown on the left side of the vertical bar) and the 373 K isotherm for reference. In addition, it shows the 600 K isotherm and the droplet evaporation rate contours. The isotherms begin on the side of the burner wall and extend into the flame because the top 1mm of the burner wall is kept at 600 K (boundary condition). The right half of Figure 4a does not show any evaporation contours because the droplets have not reached the flame base yet 0.34 sec after we started injecting the droplets.

The left half of Figure 4b shows the droplet trajectories at 0.39 sec after we began to inject the water (t=5.39 sec). The mist front is close to the 373 K isotherm. This indicates that when the droplets reach the 373 K isotherm, they begin to evaporate. However, they are completely evaporated before reaching the chain-branching reaction kernel, which is also shown in the left half of Figure 4b. The blue colored particles injected close to the burner walls are transported to the flame base and come closest to the reaction kernel. The water vapor formed by the droplet evaporation travels along the gas path lines shown in left half of Figure 4b. Therefore, the water vapor formed in front of the flame travels through the reaction kernel at the
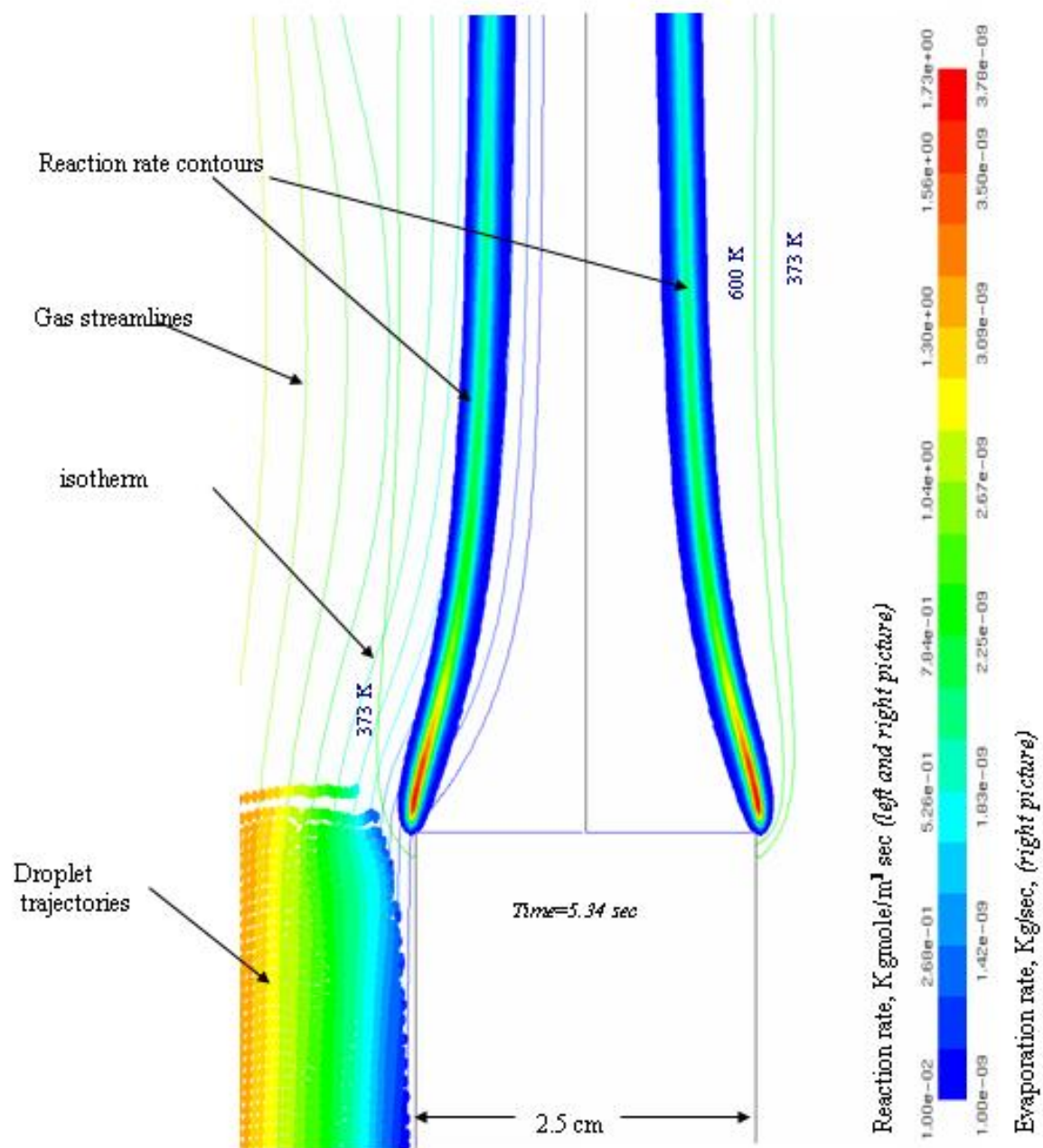
Figure 4a. Droplets did not reach the flame base at 5.34 sec: 8 μm drops, 12 mass % total water. *Left half of the burner*: Droplet trajectories, gas streamlines (color lines), and 373 K isotherm (green line) superimposed on the reaction rate contours *Right half of the burner*: Evaporation rate contours superimposed on the reaction rate contours
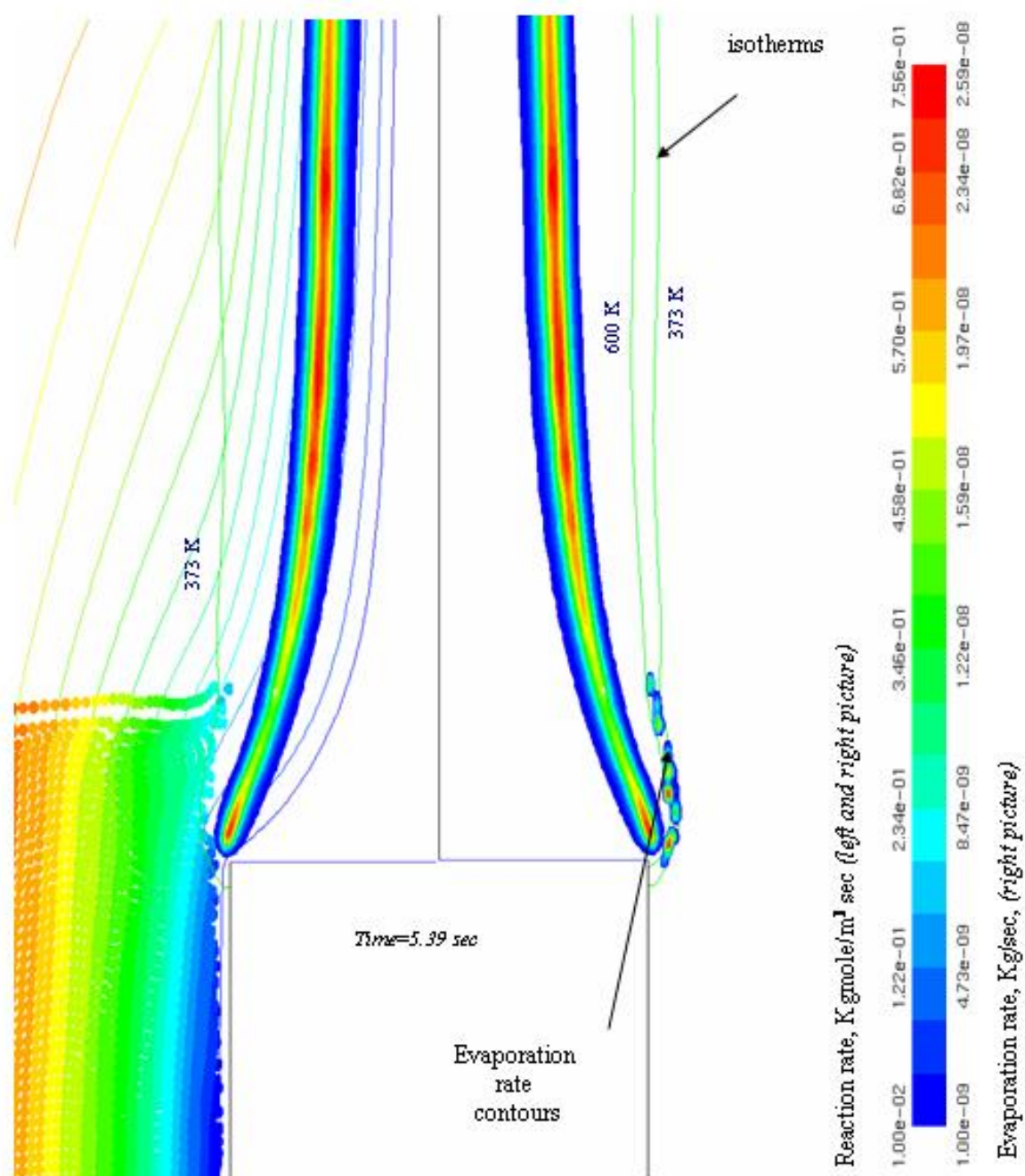
Figure 4b. Droplets evaporate between 373 and 600 K isotherms at 5.39 sec: 8 μm drops, 12 mass % total water. *Left half of the burner*: Droplet trajectories, gas streamlines (color lines), and 373 K isotherm (green line) superimposed on the reaction rate contours *Right half of the burner*: Evaporation rate contours superimposed on the reaction rate contours

flame base and dilutes the reactants. It is clear from Figure 4b that the droplet evaporation decreased the peak reaction rate in the reaction kernel significantly from 1.73 for the base case to 0.75 kgmol/m^{3}sec with droplets. Just beyond the reaction kernel, the reaction rate decreases with x due to the droplet cooling but it then increases to about the same values seen in Figure 4a in the region where droplets have not reached yet. This is shown by the red color region at large values of x. Despite this, one can see that the flame base has begun to lift up slightly from the burner rim in comparison to its position shown in Figure 4a.

        The right half of Figure 4b shows the total evaporation rate contours in relation to the reaction rate contours. The colors correspond to the magnitudes of the evaporation rate, which are displayed on the right side of the vertical bar. The effect of cooling on the reaction rate is expected to be the maximum when the evaporation and reaction rate contours overlap. The right half of Figure 4b shows that the droplet evaporation occurs between the 373 K and 600 K isotherms, and approach close to the reaction rate contours at the flame base. But, there is very little overlap between the contours. As x increases, the droplet evaporation occurs at an increasing distance from the reaction kernel as indicated by the diverging reaction and evaporation contours shown in the right half of Figure 4b. The attachment positions of the two isotherms on the burner wall have not changed significantly from those in Figure 4a.

        The left half of Figure 5a shows that the droplets have traveled about one burner-diameter distance upward at 0.54 sec after we began injecting the water (time=5.54 sec). They begin to be influenced by the buoyancy flow as indicated by the bending of the droplet and air path lines away from the reaction contours. The droplets still do not survive to reach into the reaction kernel at the flame base as in Figure 4b. However, the reaction rate contours have changed significantly from Figure 4b. The reaction kernel lifted away from the burner surface significantly and the droplets have penetrated into the flame base region between the reaction kernel and the burner rim. Also, the reaction rate decreases significantly at large values of x unlike in Figure 4b where the reaction rate is comparable to that of Figure 4a, the base-case flame. However, the reaction rate near the flame base has not changed significantly from that in Figure 4b. The right half of Figure 5a shows that the evaporation contours extend further up the axis as the droplets travel up the burner. The droplets still evaporate between the 373 K and 600 K isotherms like in Figure 4b. However, the 600 K isotherm moved up and attached at the corner of the burner rather than on the side wall as shown in the right half of Figure 4b. Therefore, the droplet cooling is significant near the burner rim. The magnitude of the evaporation rate remains about the same as in Figure 4b.
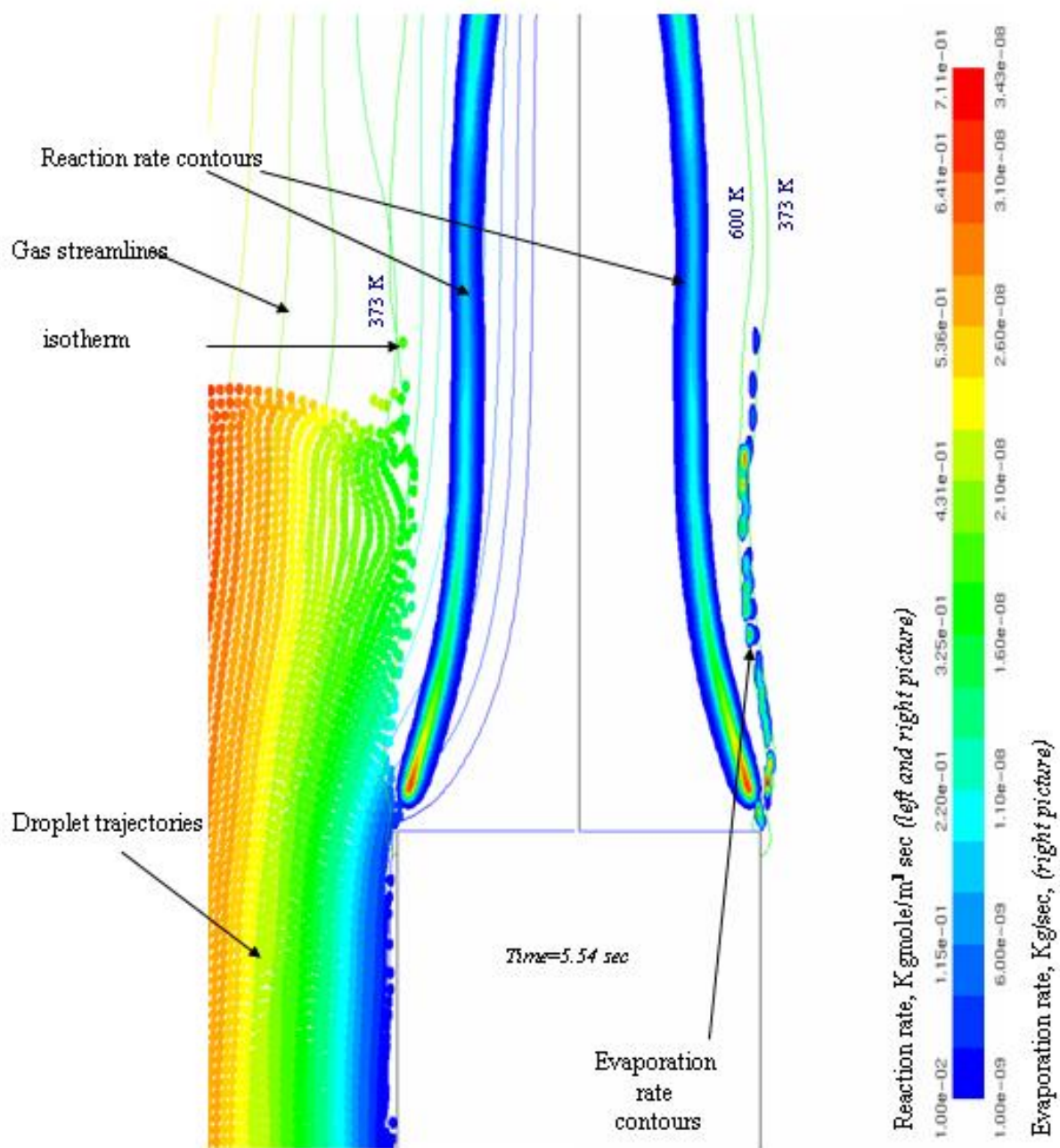
Figure 5a. Peak reaction rate decreases, the flame base lifts up from the burner at 5.54 sec: 8 μm drops, 12 mass % total water. *Left half of the burner*: Droplet trajectories, gas streamlines (color lines), and 373 K isotherm (green line) superimposed on reaction rate contours. *Right half of the burner*: Evaporation rate contours superimposed on reaction rate contours
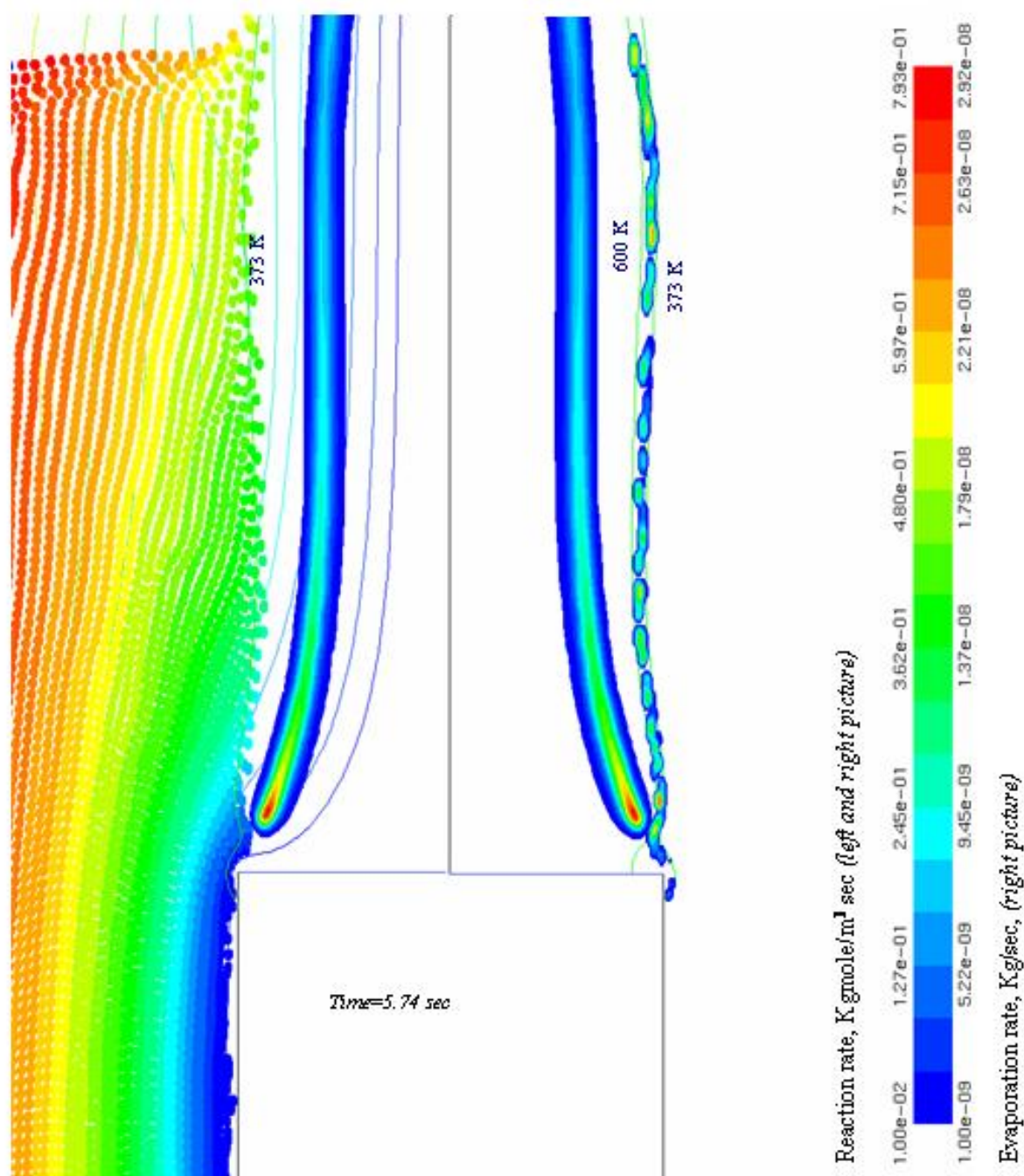
Figure 5b. Droplets begin to penetrate the region under the flame base at 5.74 sec: 8 μm drops, 12 mass % total water. *Left half of the burner*: Droplet trajectories, gas streamlines (color lines), and 373 K isotherm (green line) superimposed on reaction rate contours. *Right half of the burner*: Evaporation rate contours superimposed on reaction rate contours

The left half of Figure 5b shows droplet trajectories 0.74 sec after we began injecting water (time=5.74 sec). The droplets have traveled more than 1.5 burner diameters distance upward. The droplet trajectories deviate from the gas stream lines at the top of the picture significantly because air responds to buoyancy flow quicker than the droplets. The gas streamlines are shown as solid lines in color. However, near the flame base region, the droplet trajectories closely follow the gas stream lines. The peak reaction rate within the reaction kernel of the flame remains unchanged. However, the kernel lifts farther from the burner rim than in Figure 5a and the droplets have penetrated further into the flame base than in Figure 5a. The right half of Figure 5b shows significant evaporation in the flame base and the attachment position of the 600 K isotherm has changed significantly on to the top of the burner. The droplets still evaporate between the 373 and 600 K isotherms and the magnitude of the evaporation rate remains unchanged. Despite this, as time increases, there is slow cooling of the region between the burner rim and the reaction kernel resulting in additional flame lift away from the burner rim.

The left half of Figure 6 shows the reaction contours and the particle trajectories 0.89 sec after we began injecting water (time=5.89 sec). The droplets have reached under the flame and have begun to engulf the base of the flame. Now, the changes occur rapidly as shown by significant movement in the position of the reaction kernel, which moves up and towards the axis of symmetry. The reaction rate falls significantly to a maximum of 0.38 Kgmol/m^{3}sec in the flame tip. The water vapor formed by evaporation is entrained well into the flame and the fuel jet as indicated by the gas streamlines. The position (relative to the flame and 373 K isotherm) and the magnitude of the droplet evaporation rate remain unchanged as shown in the right half of Figure 6. Yet, significant cooling of the flame base region occurs. The 600 K isotherm attaches to the burner rim almost near the axis of symmetry. The fuel gas above a large portion of the burner exit is relatively cool. As time progresses, the flame continues to move away from the burner rim and eventually blows off.

Figures 4-6 show clearly that extinguishment occurs due to cooling of the region between the burner rim and the reaction kernel by the water droplets. The droplets injected close to the burner wall are entrained into the region near the flame base and are responsible for the extinguishment by blow-off.   The 8 μm droplets essentially evaporate between the 373 and 600 K isotherms and the rates of evaporation do not change significantly with time. Therefore, the droplets do not survive to reach the reaction kernel inside the flame base. After the droplets have traveled up and reached the burner rim, the chain-branching reaction rate decreases slowly in the initial 0.35 sec and then rapidly during the next 0.15 sec to a critical value of 0.38 Kgmol/m^{3}sec. At this point, the droplets and oxygen enter the region between the reaction kernel and the burner rim as the flame lifts away. The droplets cool the fuel mixture as well as dilute it by forming water vapor. The reaction rate is not large enough to heat the relatively cold fuel to the ignition temperature for combustion to occur. A Damkholer number can be defined as Da= δ(reaction rate/fuel flow rate), where δ is the distance between the reaction kernel and the burner rim for the base case, 0.001 m. At the extinction point, Da =0.933 for the critical reaction rate of 0.38 Kgmol/m^{3}sec and fuel flow rate of 4.07x10^{-4} Kgmol/m^{2}sec. As Da falls below a critical value, the fuel supply rate is greater than the reaction rate, and the flame moves away from the burner
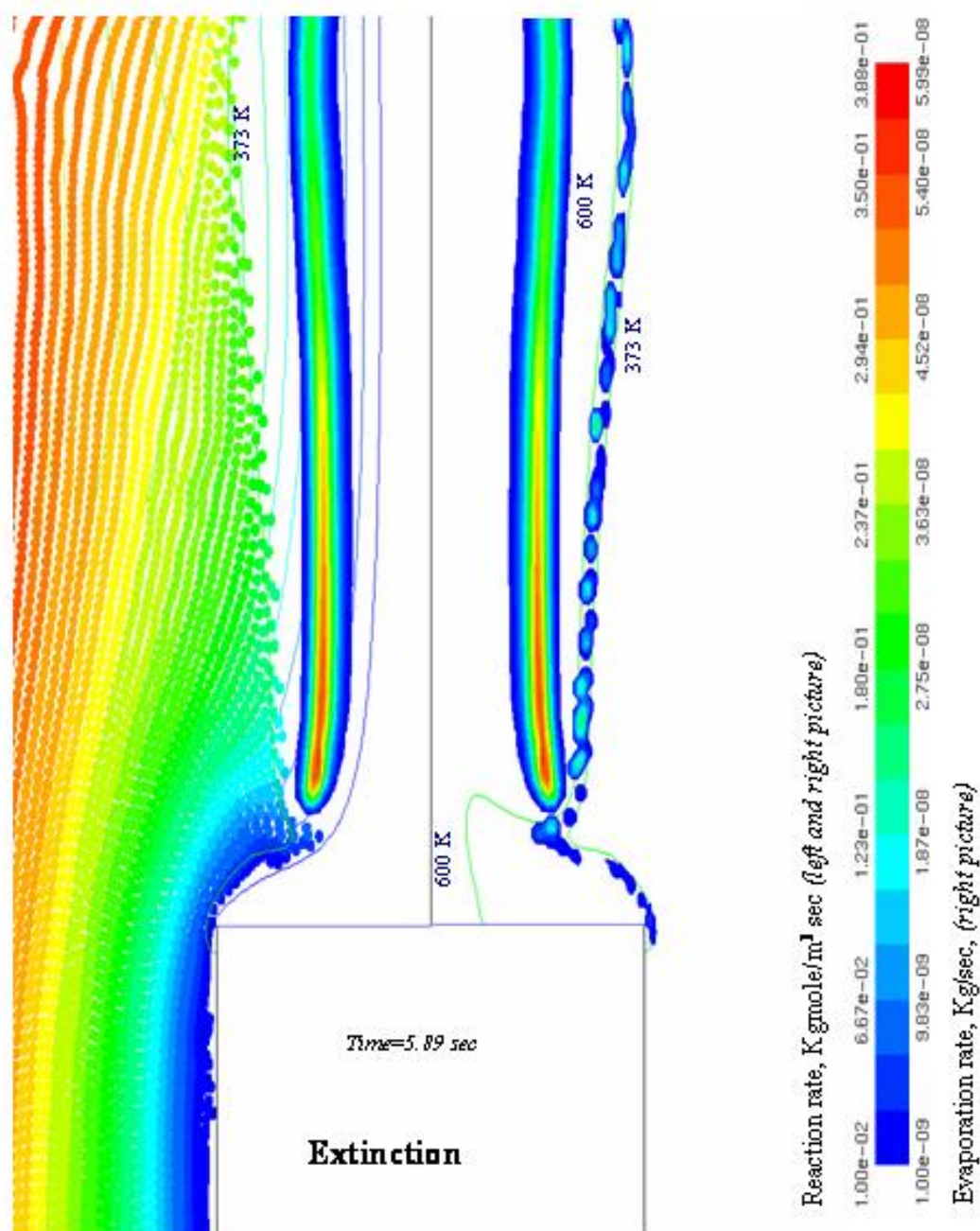
Figure 6.   8 μm drops, 12 mass% total water, droplets reach under the flame into the fuel gas, flame base separates from the burner rim and blows-off 5.89 sec.
Left half of the burner: Droplet trajectories, gas streamlines (color lines), and 373 K isotherm (green line) superimposed on reaction rate contours
Right half of the burner: Evaporation rate contours superimposed on reaction rate contours and 373K, 600 K isotherms (green lines)

rim. Therefore, the change in the reaction rate can be used as a guide to define the extinction point. We expect the critical reaction rate to be accurate within a factor of 2, since the flame did not extinguish at 0.8 Kgmol/m^{3}sec as shown later.

Figure 7a illustrates the changes in the chain-branching reaction rate further by following the reaction kernel as it moves away from the burner rim with increasing time. The kernel position is determined by locating the computational cell containing the maximum reaction rate. It occurs at x=3.18, 3.22, 3.31, 3.28, 3.84 cm at time=5.34, 5.54, 5.64, 5.74, and 5.89 sec respectively. The x values are approximate and indicate a slight degree of oscillation in the location of the peak reaction rate. Figure 7a shows the reaction rate distributions in the radial direction across the reaction kernel shown in Figures 4-6 at different times. Changes in the reaction rate occur unevenly over time before reaching the extinction value of 0.38 Kgmol/m^{3}sec at the peak. The unevenness is likely due to the discreet nature of the droplets and due to small oscillations that occur at the flame base due to flickering. The discrete drops and flame flickering cause small fluctuations in local temperature and specie concentrations. However, the key is that once the reaction rate is reduced to an insufficient level to overcome the convective and conductive heat loss, the flame continues to move towards extinction. The reaction rate will eventually decrease despite small (15 %) fluctuations along the way towards extinction. The extinction value for the reaction rate is a conservative estimate obtained from numerous computations for different drop sizes and concentrations. Similarly, Figure 7b shows the OH radical concentration distribution radially across the reaction kernel at different times. The peak OH radical concentration decreases by 43% and it plays an important role in the propagation of the combustion process. The temperature across the reaction kernel is shown in Figure 7c at different times during the extinction process.   The reaction kernel peak temperature is different from the maximum flame temperature, which occurs downstream of the reaction kernel. This is expected because it takes a short time for the gases to get heated by the release of heat within the reaction kernel and is similar to the structure reported by Ananth et al. [22]. Figure 7c shows that the reaction kernel peak temperature changes unevenly but eventually decreases by about 100 K with time. The temperature seems to increase slightly as the flame approaches extinction. Despite this slight increase, the reaction rate decreases significantly at extinction as shown in Figure 7a. Clearly, a decrease in the specie (H$_2$, O, OH, H) concentrations must be responsible for the reduced reaction rate. This could be due to the formation of water vapor that causes the dilution effect. Even though temperature is important, it is the reaction rate that affects Da directly and plays a crucial role in determining flame extinction.   To understand this fully, one must consider the energy equation, which is complex and contains many more variables than illustrated in Figures 7a-c.

Figure 8a shows the droplet concentration distribution along the three isotherms, 373 K, 500 K, and 600 K, two of which are shown in the right half of Figure 5a at time=5.54 sec. The curve length is the distance along a given isotherm, which changes with time as shown in Figures 4-6. The curve length is measured from the burner rim, and it increases with increasing values of x. Figure 8b shows the degree of droplet entrainment/evaporation along each isotherm. The droplet distributions are not smooth due to the discrete nature of the droplets at very dilute
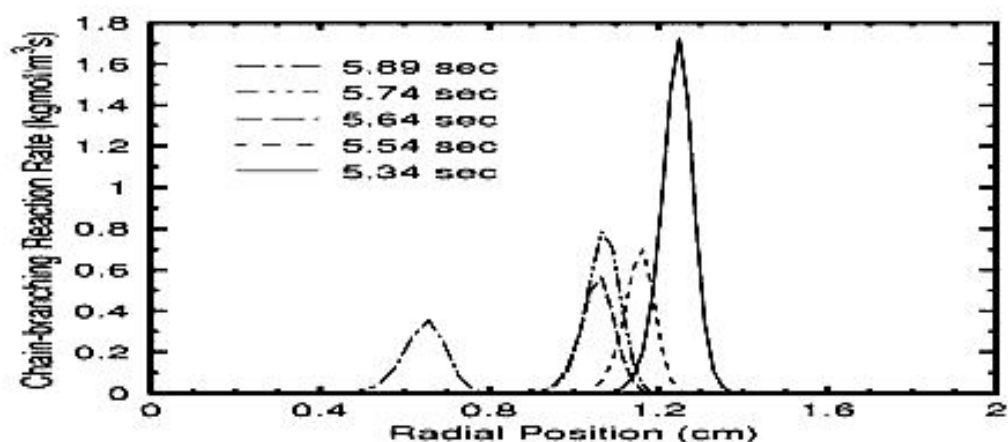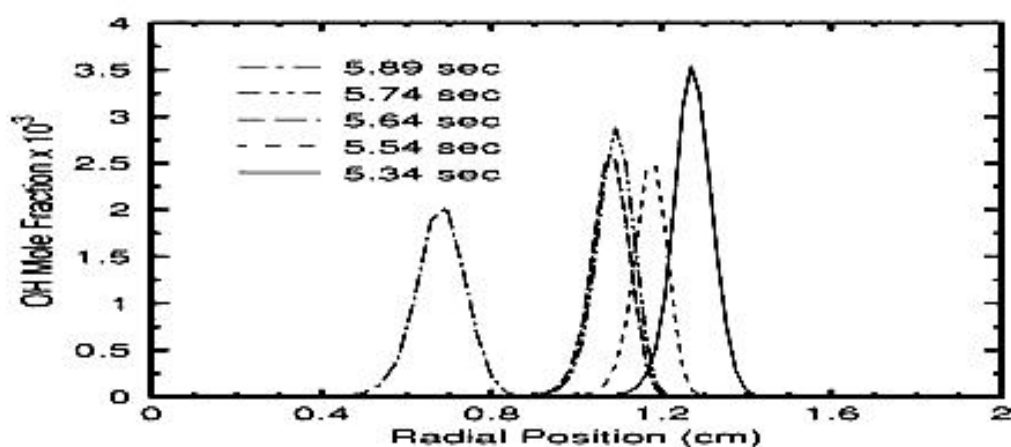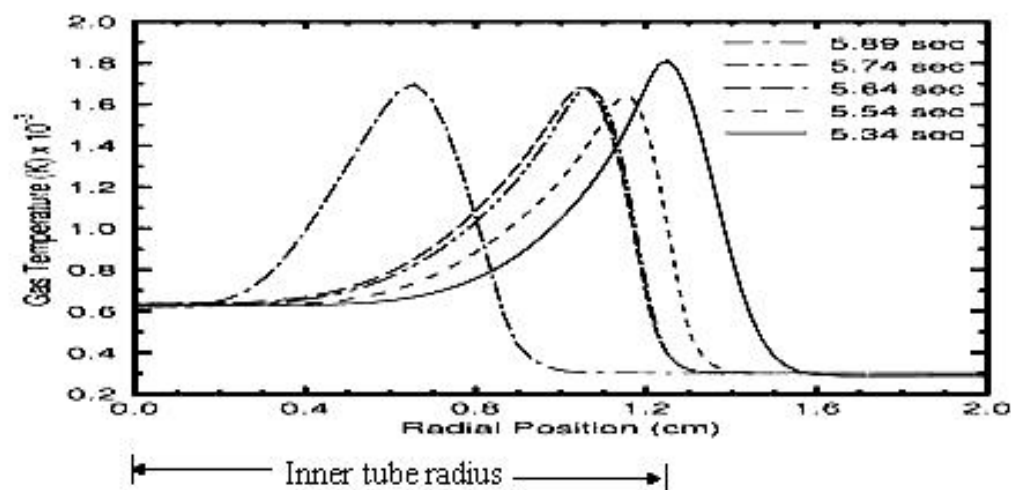
Figure 7a

Figure 7b

Figure 7c

Figure 7. Radial Distributions of reaction rate, OH, and temperature inside the reaction kernel as it moves away from the burner rim during extinction by 8 μm drops at 12 mass% total water
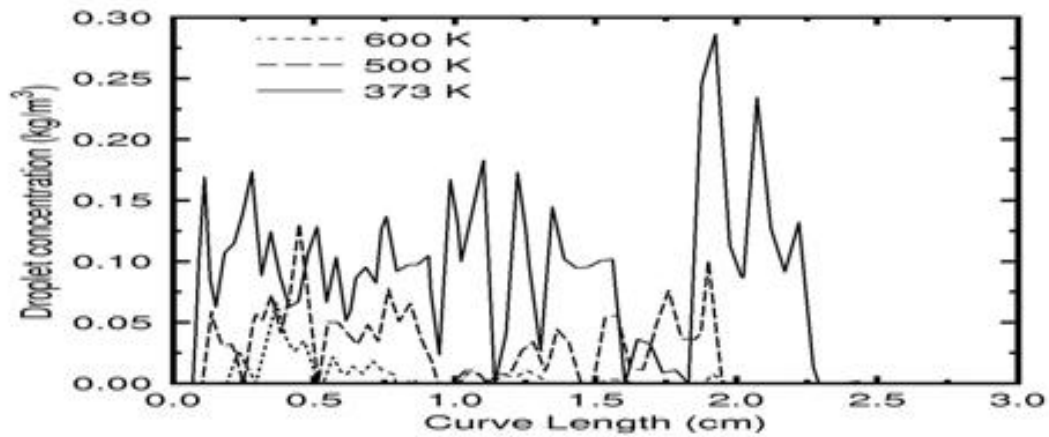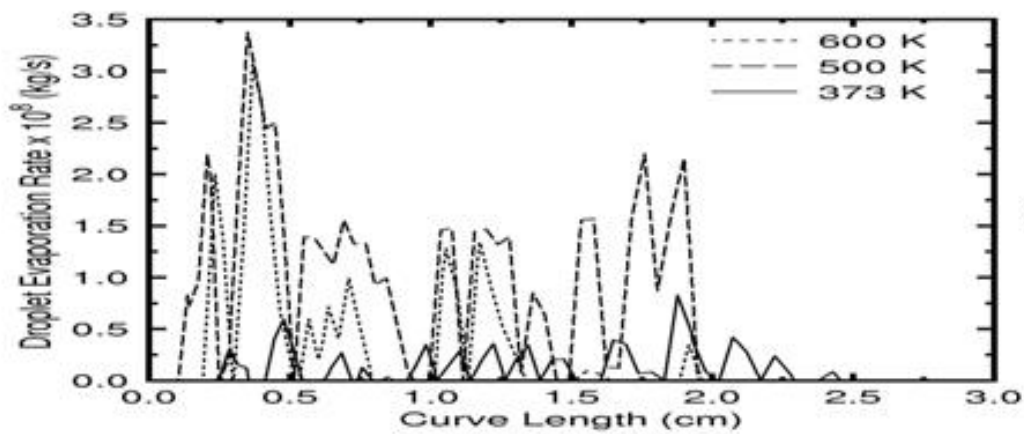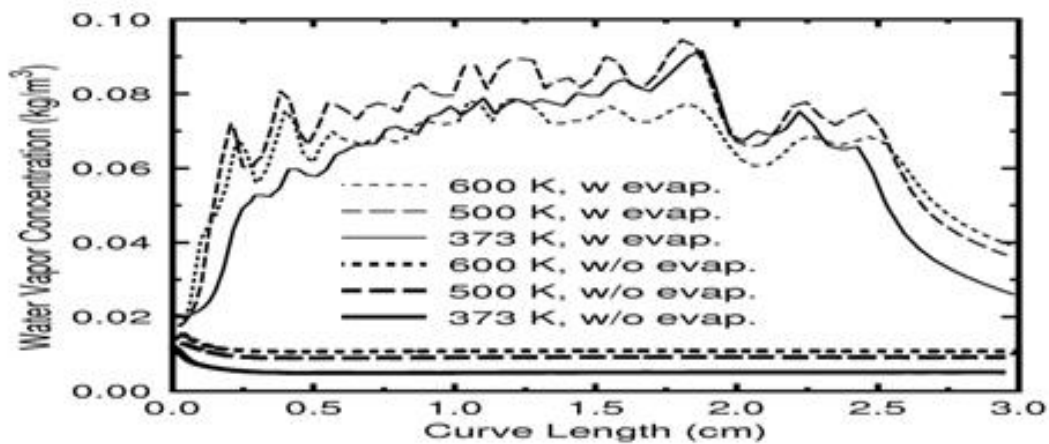
Figure 8a

Figure 8b

Figure 8c

Figure 8. Distributions of droplet concentration, evaporation rate, and water vapor along different isotherms at 5.54 sec for 8 μm drops, 12 mass% total water

concentrations by volume. As the droplets move towards the hot gases surrounding the reaction kernel, the concentration decreases continuously from 373 K to 600 K. No droplets were found along the 900 K isotherm. Figure 8b shows the evaporation rate, which is small along the 373 K isotherm and increases rapidly as the droplets penetrate toward the 500 and 600 K isotherms. As the droplets travel towards the 600 K isotherm, they reduce in size. Therefore, their evaporation rate increases despite the reduced liquid concentration shown in Figure 8a.   The evaporation rate is the degree of latent heat absorption from the hot gases. As the evaporation rate increases, the water vapor concentration increases which causes dilution of oxygen and other species and hinders combustion. Figure 8c shows the water vapor concentration due to the combined effects of vaporization and the formation of water from the combustion chemistry. In an attempt to separate the two phenomena, we also show water vapor concentrations at a time (5.24 sec) before the droplets begin to interact with the flame base. These correspond closely to the base case, where water vapor is formed solely due to combustion of propane. Figure 8c shows clearly that the water vapor formed by the combustion process (i.e., "w/o evap") is significantly smaller than that formed by the droplet evaporation. Therefore, evaporation is a key factor in achieving extinction by oxygen dilution and sensible heat absorption by the water vapor, which has much higher specific heat than air.

At a slightly higher droplet concentration of 12.2 mass % (+ 1.8% vapor, i.e., 14 mass % total water) than the extinction concentration (12 mass % total water), which is shown in Figures 4-6, the extinction process occurs rather rapidly. The droplets were injected at the air inlet exactly same as in Figures 4-6. From our computations, we observed that the reaction kernel at the flame base begins to detach from the rim, when the droplets injected adjacent to the inner tube wall reach the burner rim at time=5.49 sec. At time=5.59 sec, the peak reaction rate in the reaction kernel at the flame base falls from 1.8 to 0.33 kgmol/m^{3}sec, and the kernel moves up from 1 mm to 3.3 mm above the rim. Figure 9a shows the simulation results for flame position for 14 mass % total water at time= 5.69 sec. The reaction kernel moves up about 8.5 mm from the rim as shown in Figure 9a. As the time progresses further, the flame continues to move away from the burner, and blow-off occurs. The left half of Figure 9a shows that the droplets follow the air stream lines closely and enter the region underneath the reaction kernel into the fuel core. However, the droplets still do not enter into the reaction kernel at the flame base. They penetrate slightly past the 373 K isotherm similar to the results displayed in Figure 6.   The local cooling by the droplets leads to the decrease in the reaction rate inside the kernel, which is surrounded by the water droplets. However, the reaction rate away from the kernel increases with x and reaches about 0.67 Kgmol/m^{3}sec as indicated by the red colored region at the top in the left half of Figure 9a. In this region, the droplets have not reached the flame yet and local cooling does not occur. The right half of Figure 9a shows clearly that the local cooling by the droplets injected very close to the burner wall plays a key role in reducing the local reaction rate inside the kernel. The reaction rate inside the kernel is the key parameter that controls the extinction by blow-off from the burner rim.
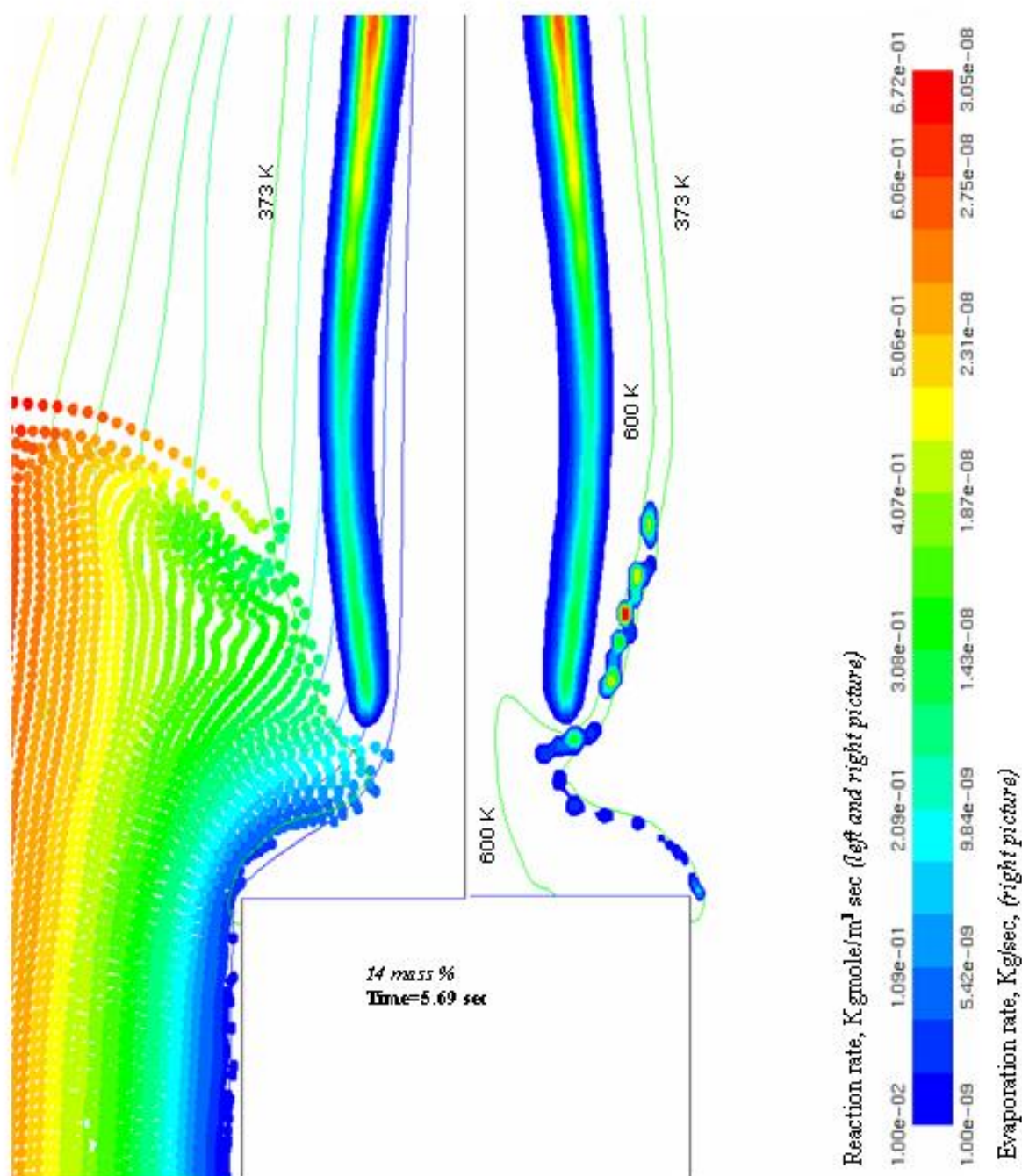
Figure 9a. 8 μm drops: Extinction at droplet concentration (14 mass % total water) above the extinction concentration *Left half of the burner*: Droplet trajectories, gas streamlines (color lines), and 373 K isotherm (green line) superimposed on reaction rate contours *Right half of the burner*: Evaporation rate contours superimposed on reaction rate contours

Figure 9b. 8 μm drops: No extinction below (9 mass % total water) the critical droplet concentration. *Left half of the burner*: Droplet trajectories, gas streamlines (color lines), and 373 K isotherm (green line) superimposed on reaction rate contours *Right half of the burner*: Evaporation rate contours superimposed on reaction rate contours
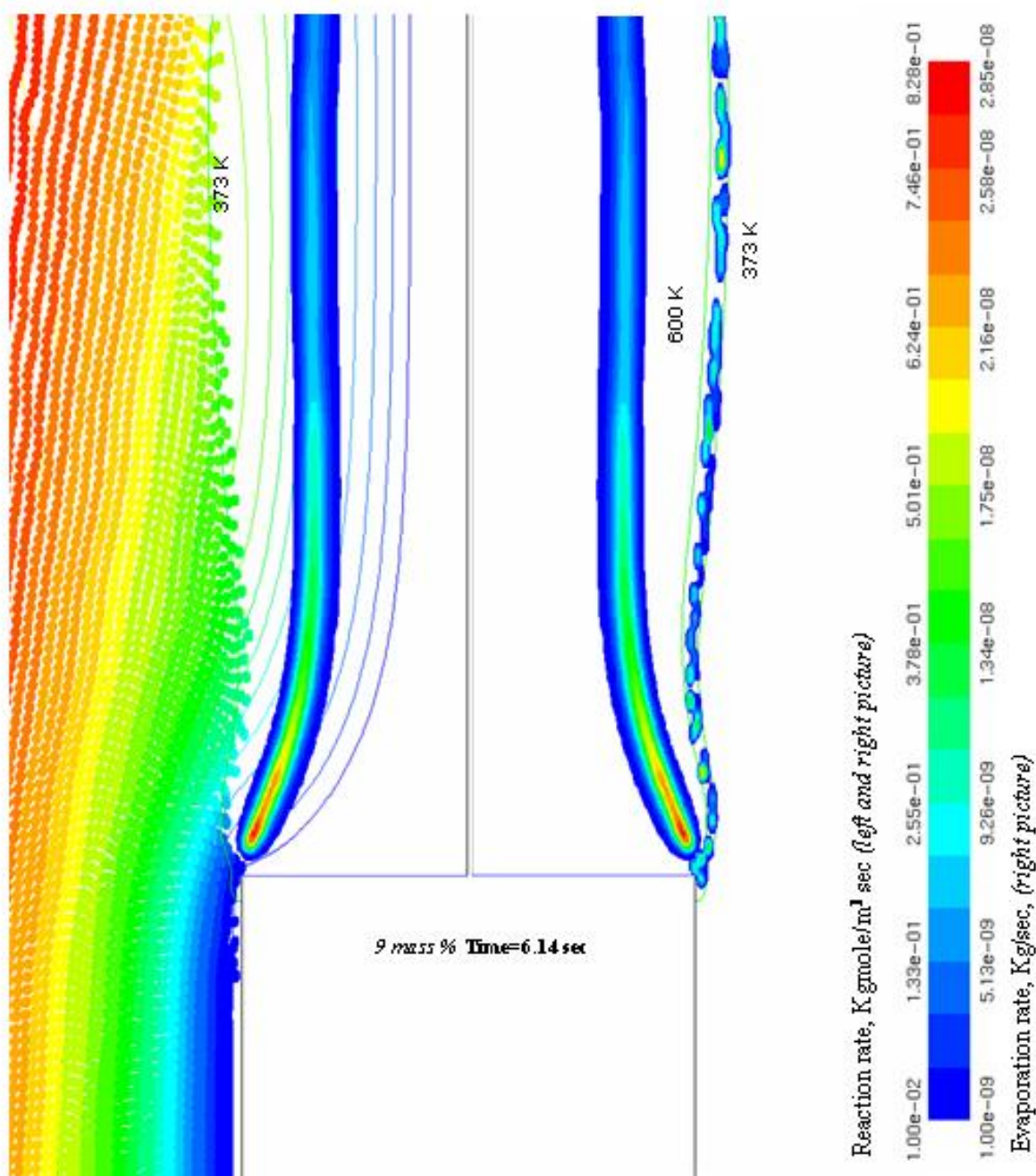
The evaporation rate contours displayed in the right half of Figure 9a are very similar to those in Figure 6 and are again bounded between the 373 and 600 K isotherms. Clearly, increasing the droplet concentration did not enable the droplets to penetrate any further into the reaction core. The 600 K isotherm moved up and towards the axis of symmetry significantly due to cooling of the region above the burner rim by the droplet evaporation like in Figure 6. The right hand side of the vertical bar displays the magnitudes of the evaporation rate, which is similar to that in Figure 6 because the droplet concentrations differ only by 20%.

The left half of Figure 9b displays the droplet trajectories and the chain-branching reaction rate contours at droplet concentration of 7.2 mass % (+ 1.8% vapor, i.e., 9 mass % total water) in the inlet air. The computations showed that the flame does not extinguish at 9 mass % total water concentration as shown in Figure 9b. The droplets cool the flame and the reaction kernel detaches slightly from the rim as in Figure 5a. But, the flame remains stable, attached at the new location, and remains unchanged with time unlike the extinction process displayed in Figure 6. The droplet cooling leads to a reduction in the reaction rate to 0.83 kgmol/m^{3}sec, which is well above the approximate extinction limit of 0.38 kgmol/m^{3}sec. The peak reaction rate inside the kernel decreases with x as shown in Figure 9b. The droplets (blue colored) injected adjacent to the burner wall entrain towards the flame base but do not penetrate significantly the region between the reaction kernel and the burner rim. The right half of Figure 9b is similar to Figure 5a and shows that the 600 K isotherm moved up to the corner of the burner. But, the isotherm in Figure 9b remains unchanged with time. Despite lower droplet concentration, the droplets evaporate between the 373 and 600 K isotherms and the evaporation rates are comparable to those displayed in the right half of Figure 5a. Clearly, the location for complete evaporation of the droplets is determined by the droplet diameter rather than the droplet concentration.

Figures 4-6 and 9a show that the droplets reduce the chain-branching reaction rate inside the reaction kernel below a critical value (0.38 kgmol/m^{3}sec) at flame extinction. In Figure 10, we show that the maximum local reaction rate decreases with time for three different droplet concentrations. The extinction time is defined as the time needed for the reaction rate to fall to the critical value. Therefore, Figure 10 shows that the extinction time is 0.55 sec, at 12 mass % total water (drops+vapor). At the critical reaction rate, the extinction time decreases by a factor of 3.6 as the total water concentration is increased from 12 mass % to 14 mass %. At 9 mass % total water, the reaction rate does not reach the critical value and the flame is not extinguished even after 1 sec. In Figure 10, the time is measured from the point at which the droplets adjacent to the burner wall are about to reach the burner rim (e.g., Figure 4a) and the droplets begin to evaporate and interact with the flame tip. Therefore, the time does not include the time required for the droplets to travel up to the flame base.
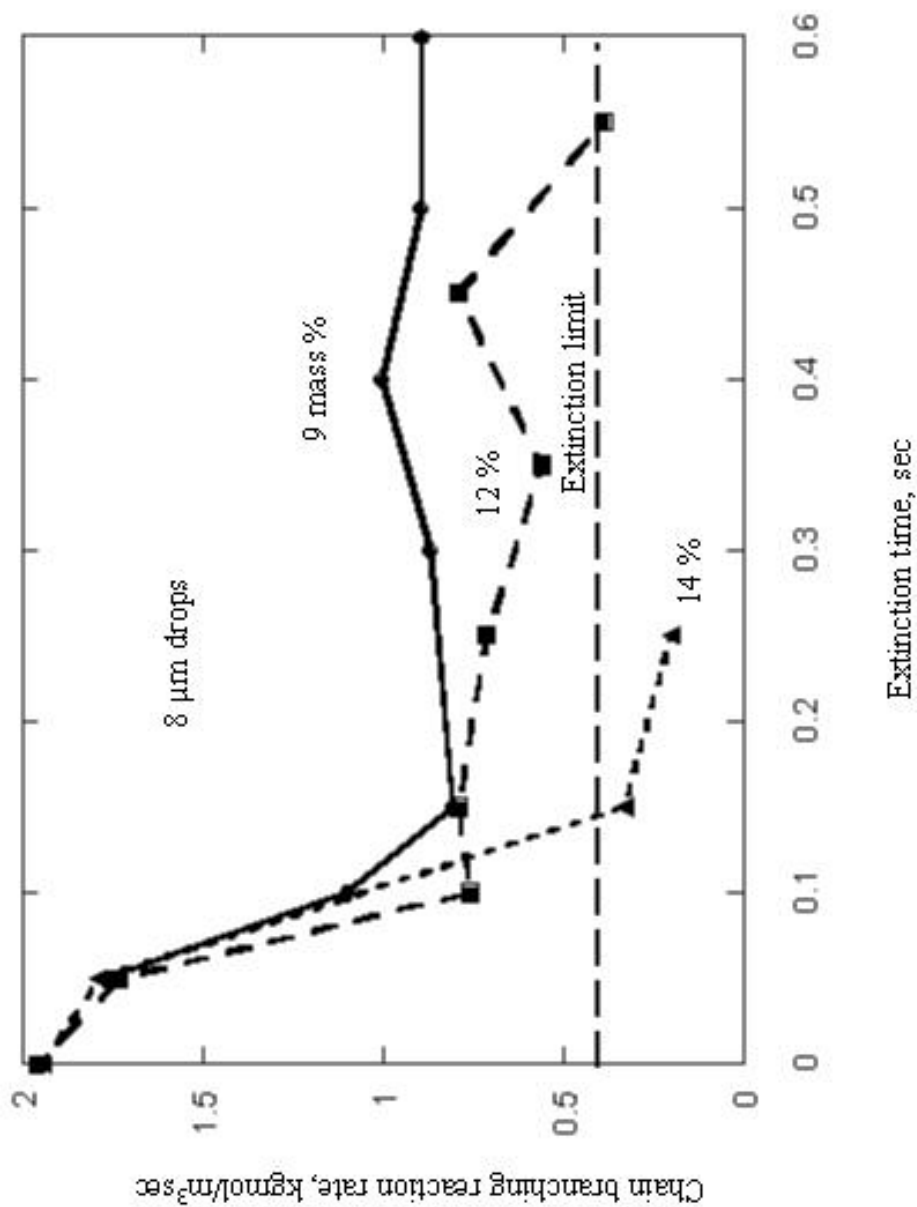
Figure 10. Effect of total-water (droplets+1.8% vapor) concentration on the chain-branching reaction rate inside the reaction kernel as it moves away from the burner rim with time

In practice, mist formed by nozzles or ultrasound instruments contains a distribution of droplet sizes. The evaporation rate is directly related to droplet size. Therefore, the effects of droplet size will be examined next. We inject 32 μm, mono-dispersed, droplets at 8.7 mass % droplet concentration (10.5% total water) with the air (100 % humidity or 1.8 mass % water vapor) at the entrance of the burner similar to the injections in Figure 4a. After the injection, the droplets travel up and reach the burner rim (at time=5.59 sec) more slowly than the 8 μm drops. The left half of Figure 11a shows the droplet trajectories, the reaction rate contours, and the 373 K isotherm 0.89 sec after we injected water (time=5.89 sec) at extinction. The droplet trajectories deviate more from the air stream lines than the 8 μm drops shown in Figure 6. This is evident even near the flame base region, where the droplets seem to bend downward towards the burner surface slightly. This is due to a larger gravity effect on the droplet momentum than for the 8 μm drops. More importantly, the droplets penetrate the flame significantly farther, surviving well past the 373 K isotherm, and reach into the reaction kernel at the flame base unlike in Figure 6. The reaction rate drops well below the critical value to 0.26 kgmol/m^{3}sec inside the reaction kernel, which is located about 7 mm above the burner rim. Clearly, the kernel is well surrounded by the droplets as they enter under it into the core of the fuel jet.

Figure 11a clearly shows that 32 μm drops are more effective than 8 μm drops. This is surprising since larger drops evaporate slower than the small drops according to the d^2-law. The reason for the higher effectiveness of large drops can be seen in the right half of Figure 11a. The right half of Figure 11a shows the evaporation rate contours in relation to the reaction rate contours. There is now a significant overlap between the two contours near the flame base unlike in Figure 6, which is for the 8 μm drops. One might expect that droplet sizes slightly larger than 32 μm might be optimum, and result in complete overlap between the reaction rate and evaporation rate contours. The droplet evaporation rate contours are also thicker for 32 μm drops than for 8 μm drops. A comparison of Figures 11a and 6 shows that the bigger drops evaporate partly inside of the reaction kernel while the smaller drops evaporate completely outside of the kernel region. Therefore, for 32 μm drops, the latent heat absorption occurs partially inside the reaction kernel directly leading to reduction in the maximum local reaction rate well below the critical value needed for flame extinction. The right half of Figure 11a also shows the 373, 600, 900, and 1200 K isotherms. Clearly, droplet evaporation occurs well past the 600 K isotherm and up to the 1200 K isotherm. The magnitude of the evaporation rates is significantly smaller in Figure 11a than in Figure 6. The smaller evaporation rates are due to reduced surface-area-to-volume ratio as the droplet size is increased. Despite the reduced evaporation rate, the flame is extinguished at 8.7 mass % droplet concentration (+1.8 % vapor) for 32 μm compared to 10.2 mass % (+1.8 % vapor) needed for 8 μm drops. For the large drops, the evaporation of drops inside the reaction kernel of the flame base plays a significant role in the droplet effectiveness in extinguishing the flame. Computations at droplet concentrations of 7.2 mass % (+1.8 % vapor) do not lead to flame extinguishment.

The left half of Figure 11b shows the droplet trajectories and the reaction rate contours for 4 μm drops injected with the air at a droplet concentration of 14.2 mass % (+1.8 % vapor, i.e., 16 mass % total water). It shows that the droplets do not reach into the reaction kernel. But, the
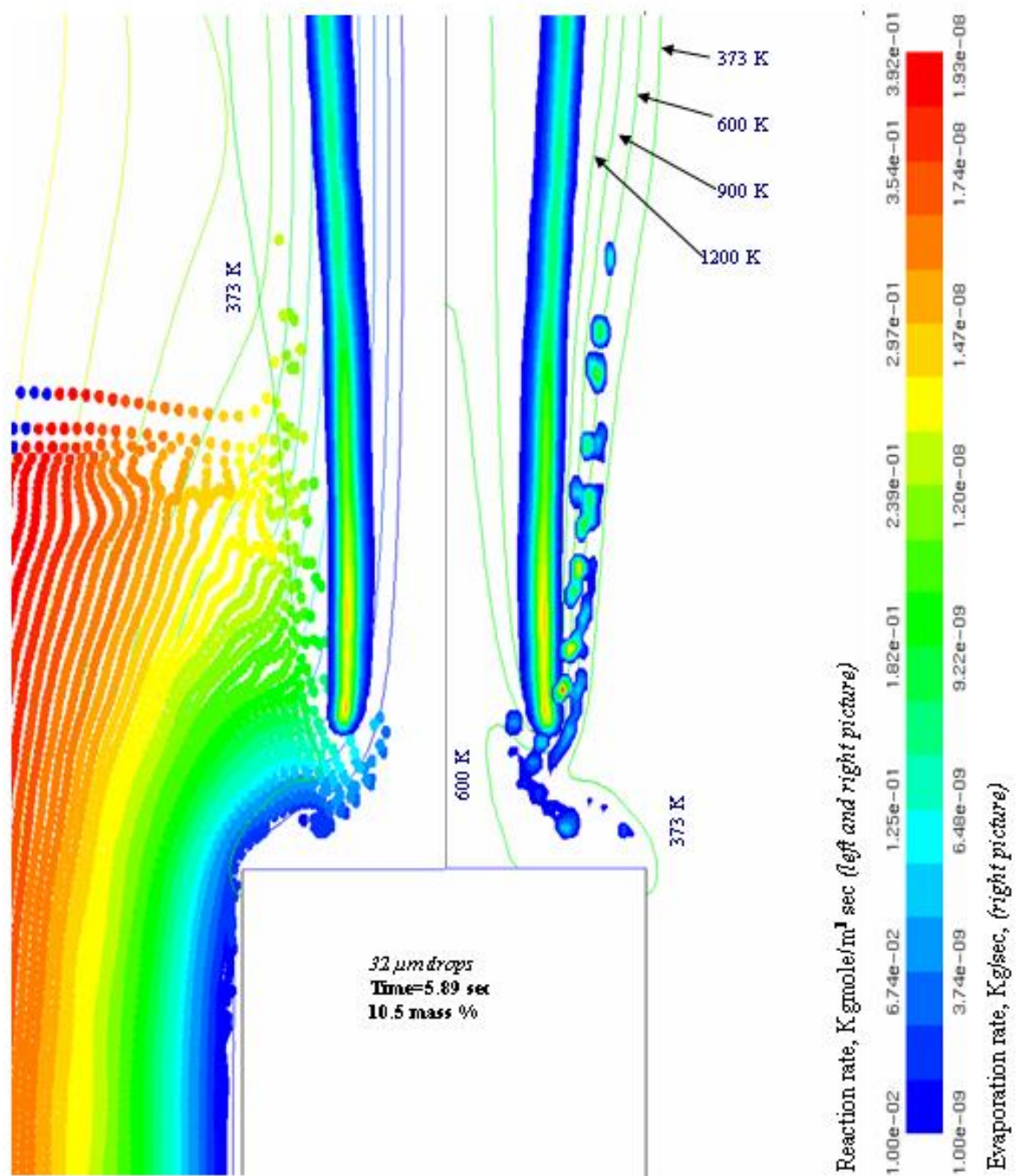
Figure 11a. Large drops (32 μm) survive up to 1200 K isotherm, and evaporation rate contours partially overlap with the reaction rate contours.. *Left half of the burner*: Droplet trajectories, gas streamlines (color lines) superimposed on reaction rate contours. *Right half of the burner*: Evaporation rate contours superimposed on reaction rate contours and the isotherms (green lines)

Reaction rate, Kgmole/m³ sec (left and right picture)

1.00e-02 6.48e-02 1.20e-01 1.74e-01 2.29e-01 2.84e-01 3.39e-01 3.76e-01

Evaporation rate, Kg/sec, (right picture)

1.00e-09 7.19e-09 1.34e-08 1.96e-08 2.58e-08 3.19e-08 3.81e-08 4.23e-08

4 µm drops
Time=6.14 sec
16 mass %

600 K

373 K

Figure 11b. Small drops (4um) evaporate relatively farther from the reaction rate contours. *Left half of the burner*: Droplet trajectories, gas streamlines (color lines) superimposed on reaction rate contours. *Right half of the burner*: Evaporation rate contours superimposed on reaction rate contours and the isotherms (green lines)
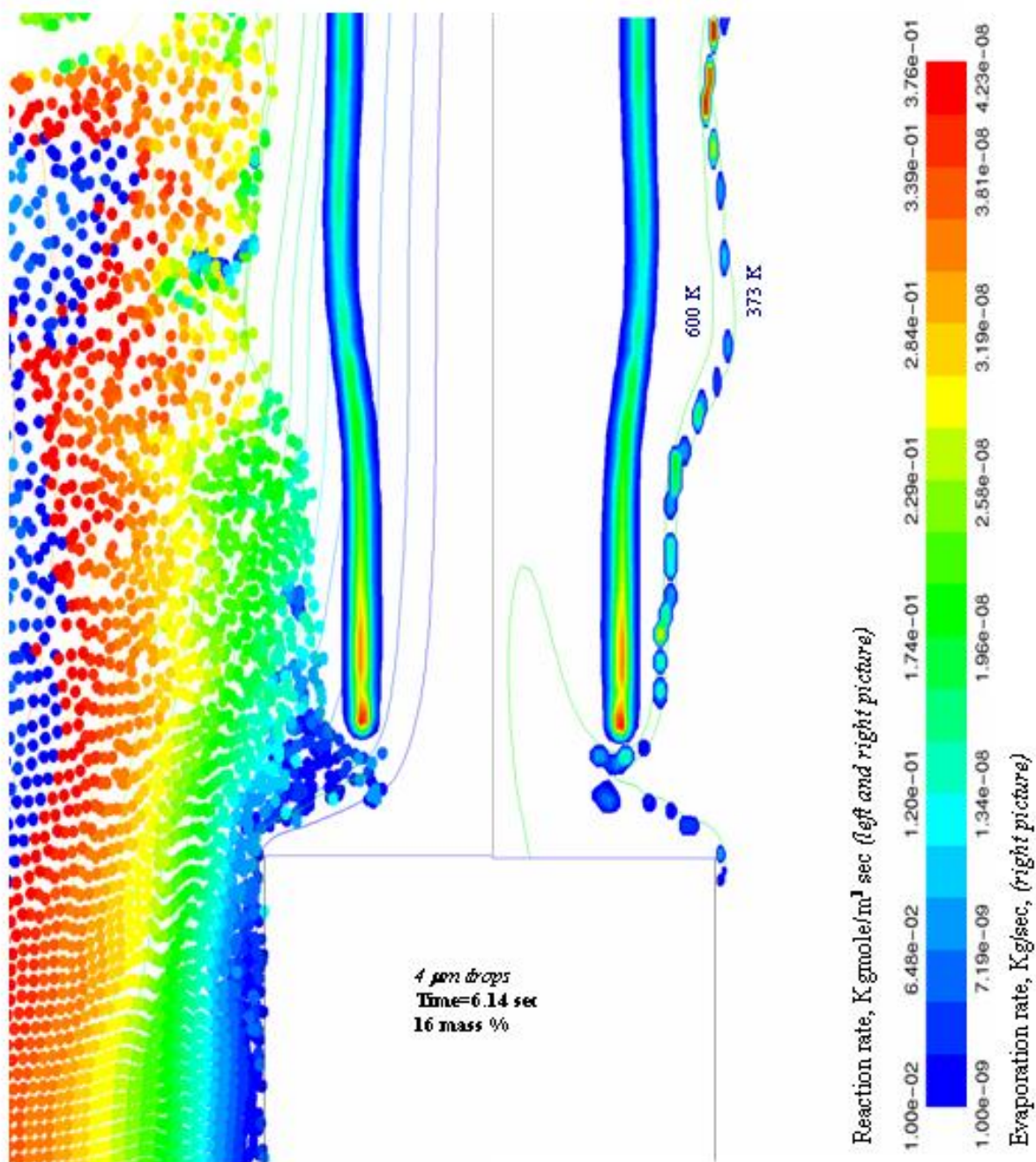
35

cooling of the region between the kernel and the burner rim is significant at this concentration of the drops and leads to a significant reduction in the maximum reaction rates to 0.38 kgmol/m³sec inside the reaction kernel. The water vapor formed by evaporation follows the gas path lines and is entrained into the kernel. This dilutes the fuel-air mixture around the reaction kernel and lowers the reaction rate. The dilution effect may be more important for the small-size drops than for large drops. The cooling and dilution extinguishes the flame by blow-off as before. The right half of Figure 11b shows that the droplets evaporate between the 373 and 600 K isotherms and the evaporation is well outside the reaction kernel like in Figure 6 for the 8 μm drops. Computations performed at 12.2 mass % droplets (+1.8 % vapor) did not extinguish the flame because it is below the critical concentration of 16 mass % total.

Figure 12a and b compare evaporation rates along different isotherms for 32 and 4 μm drops at time=5.69 and 5.79 sec respectively, and at their respective values of the extinction concentration in mass %. Clearly, the evaporation rates are significantly higher for the small drops than the large drops. But, for 4 μm drops, the evaporation occurs along the 373 K, 500 K and 600 K isotherms, which are farther from the reaction kernel than 1200 K isotherm. For 32 μm drops, significant evaporation occurs even at the 1200 K isotherm, which is close to the reaction kernel of the flame base. More importantly, the evaporation rate and reaction rate contours begin to overlap for 32 μm drops as shown in the right half of Figure 11a. Therefore, significantly less water is needed to extinguish the flame for 32 μm drops than for 4 μm drops. Unlike the 4 μm drops very little evaporation occurred at 373 K isotherm for 32 μm drops as shown in Figure 12a. Also, no droplets survived at 1500 K for 32 μm drops.

Figure 13 shows the maximum local reaction rate inside the reaction kernel, as it detaches from the burner rim, with time for different droplet diameters at their extinction concentrations. The reaction rates fall to the critical value, 0.38 kgmol/m³sec, within 1 sec. Clearly, as the droplet size is increased, they become more effective in extinguishing the flame in the size range studied. The extinction time is very sensitive to the droplet concentration near extinction. A small change in the concentration can lead to significant changes in extinction time. This results in the somewhat non-smooth behavior in the extinction curves shown in Figure 13.
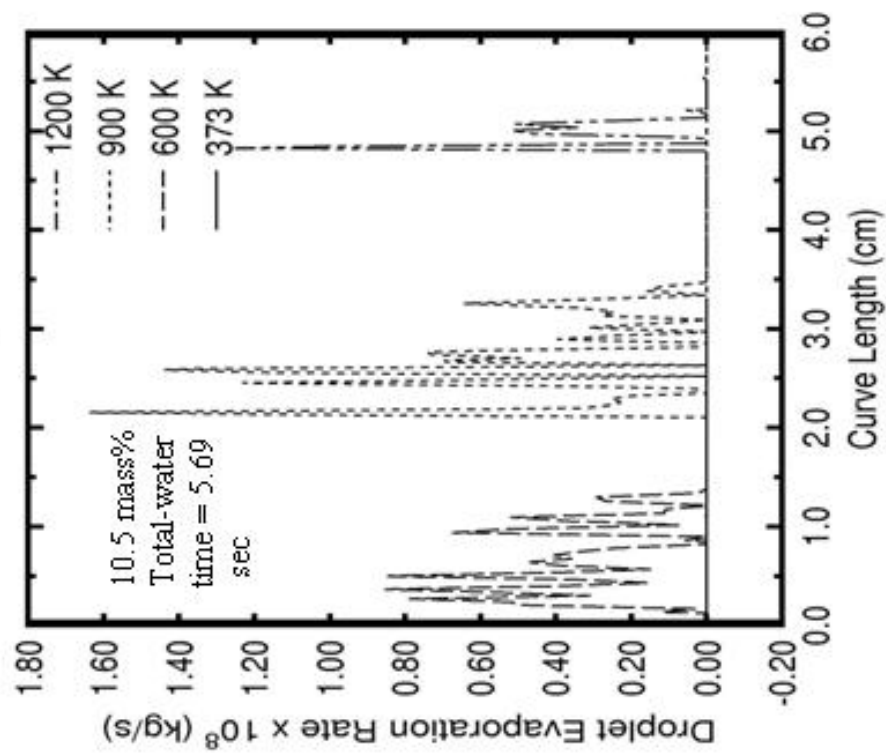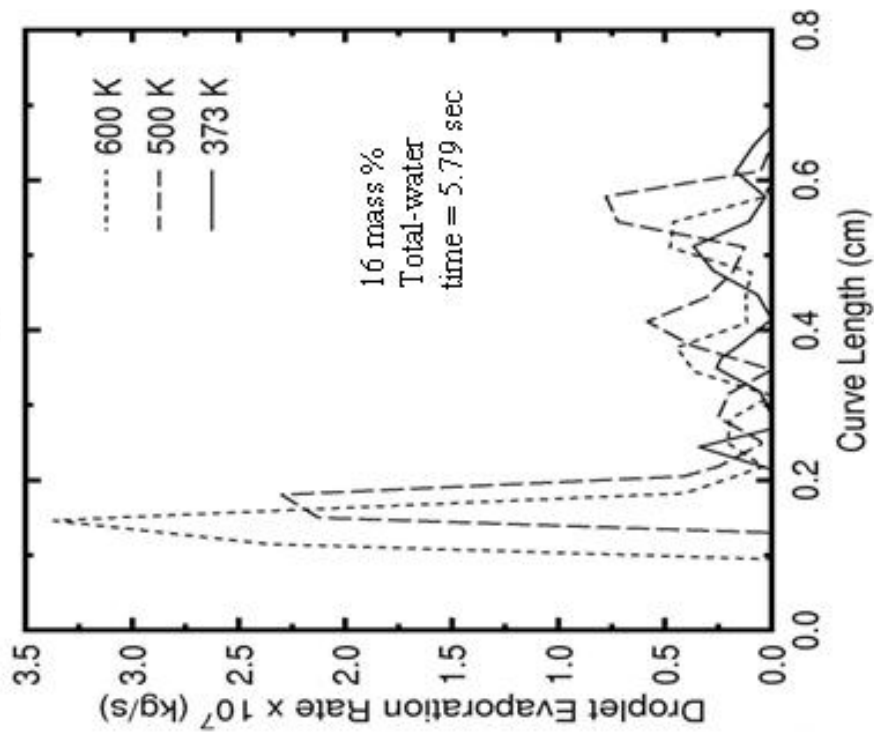
Figure 12 b

Figure 12 a

Figure 12.   Comparison of evaporation rates for 32 and 4 μm drops along different isotherms at extinction
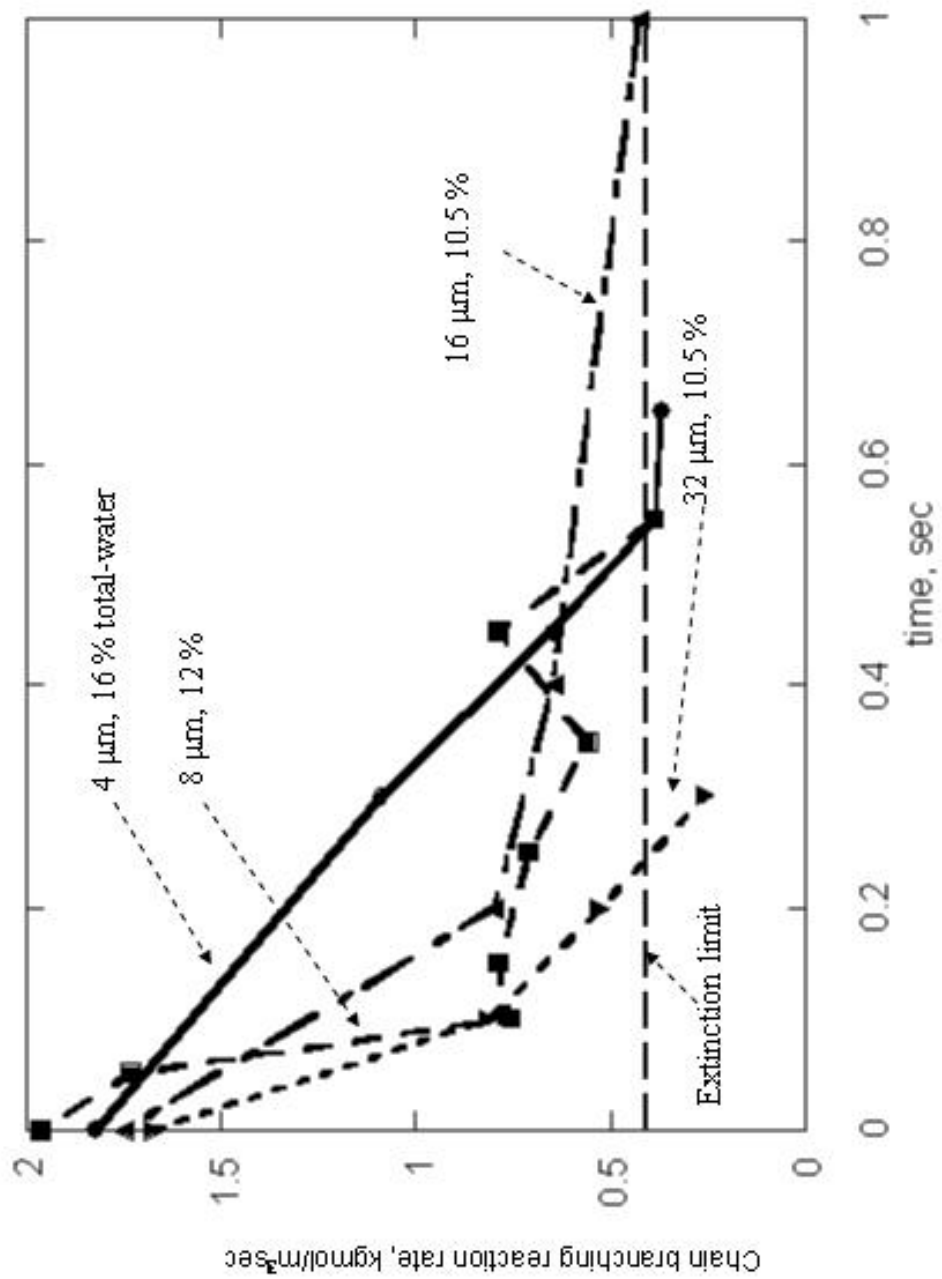
Figure 13. Effect of droplet size on the chain-branching reaction rate inside the reaction kernel as it moves away from the burner rim with time

Figure 14 shows the extinction concentrations in terms of total water (droplets+1.8% vapor) for different size droplets. It shows that the extinction concentration increases by 40% as the droplet size decreases from 32 to 4 μm. The large drops are more effective even though evaporation occurs within the hot region of the flame for all drop sizes examined. This is counter intuitive because one might expect that the large drops evaporate slower than the small drops due to their small surface-area-to-volume ratio. Our computations show that this enhanced effectiveness is due to the ability of the large drops to survive passage through the thermal layer and penetrate into the reaction kernel at the flame base. This is illustrated by the better overlap between the evaporation and reaction rate contours shown in Figure 11a. Therefore, there is a competition between degree of droplet penetration into the reaction kernel and the droplet evaporation rate. Extremely small droplets evaporate faster than large drops, but they do not penetrate the reaction kernel significantly. Very large drops (larger than those considered in the present computations), on the other hand, penetrate the reaction kernel, but are too slow to evaporate. Our computations for 45 μm droplets showed severe deviations between the droplet trajectories and the air entrainment path lines due to gravity, and the droplets begin to fall into the burner (inner tube). Therefore, the computations were discontinued. However, we expect that a further increase in size (with an appropriate increase in injection velocity) will lead to droplet evaporation that overshoots the reaction kernel at the flame base. As the size increases the evaporation rates decrease and the drops are expected to reach past the reaction kernel inside the fuel jet. Therefore, they will be less effective in extinguishing the flame as the size is increased beyond 45 μm. That would be consistent with the computations performed by Prasad et al. [9] for methane combustion in a slot burner for droplet sizes of 50 to 150 μm. They showed that the extinction concentration increases from 17.5 to 50 mass % as the droplet size is increased from 50 to 150 μm. The flow velocities of air and fuel are higher than those used in the present study. This permitted studies of large droplets by Prasad et al. [9]. The non-monotonic behavior in droplet concentration (at extinction) with drop size in 2-dimensional, low strain, co-flow flame appears to be qualitatively similar to the relationship between extinction strain rate and drop size predicted for 1-dimensional, highly strained, opposed jet flame considered by Lentati and Chelliah [24, 25]. Further work is needed to establish a quantitative relationship between these two works.

Recently, co-flow experiments on the interaction of water drops with a propane diffusion flame were performed by Fisher et al. [27] by injecting ultra-fine mist having a very narrow size distribution. The air and fuel-flow rates, and the size of the burner are very similar to that used in our computations. Their Figure 4 of the flame and the particle trajectories show that the 5 μm droplets evaporate in front of the flame image. No droplets were found inside the flame image at very low concentrations (<3 %) used in the imaging experiments. This appears to be similar to the present computations of particle paths and reaction rate contours presented in the left half of Figure 11b for 4 μm drops, which are shown to evaporate completely well outside the reaction kernel. They also measured the extinction concentration for very fine poly-dispersed mist (D_{10}=6.2 μm) generated by an ultrasound method to be 12.5 % drops (+1.4% vapor +1.8% nitrogen) by mass. Our computations for 4 μm and 8 μm drops predict an extinction concentration of 13.2% drops (+1.8% vapor) and 10.2% drops (+1.8% vapor) respectively. Clearly, the measurements are well bounded by the predictions from our computations. Also,
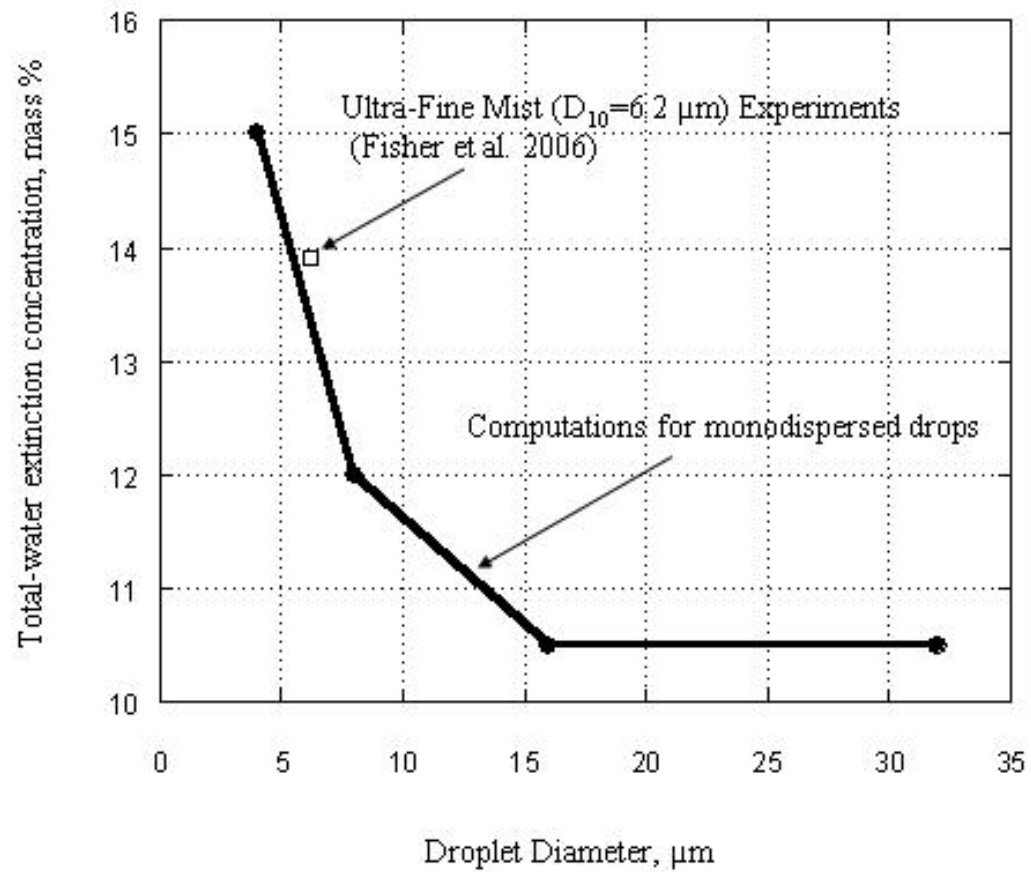
Figure 14. Droplet size effect on total-water extinction concentration and comparison with experiments

Figure 14 shows excellent agreement between the data of Fisher et al. [27] and our present computations for the extinction concentrations, assuming that the polydispersed UFM is equivalent to monodispersed mist with droplet diameters equal to experimentally measured D_{10}=6.2 µm values. However, detailed experimental measurements for temperature and water vapor and computations for polydisperse mist may be needed to understand the experiments of Fisher et al. [27]. It is also interesting that the predicted extinction droplet concentration is also consistent with the measurements of Shilling et al. [29] for water mist extinction of a heptane pool inside a cup-burner. If the polydispersity of the mist is large, the large drops may stagger behind small drops due to differences in drag and gravity effects, which may affect the detachment dynamics of the flame base.

Ananth et al. [22] predicted that 9.5 mass % ultra-fine mist (includes 1.8% vapor) is needed to extinguish a boundary layer flame formed over a PMMA plate at bulk air velocity of 60 cm/sec. Extrapolating their calculations to zero air velocity gives an extinction water concentration of 12.5 mass %. Extrapolation of the measurements by Ndubizu et al. [18-20] of the extinction mist concentration also gives similar results. This extinction value for PMMA flame is only slightly smaller than the values shown in Figure 9a for 4 to 8 µm drops for the co-flow geometry. This further confirms that the transport phenomena near the flame attachment region (flame base for co-flow and leading edge for boundary layer) are of key importance for extinguishment over other factors.

Finally, the difference in the extinction concentrations for water and water vapor show the effect of latent heat. For example, 12 mass % is needed for extinction with water mist with 8 µm drop sizes, while 17 to 20% mass % is required for water vapor. Therefore, the absence of the latent heat effect results in a need for about 5 to 7% extra vapor to extinguish the flame. Similarly, the absence of a difference in specific heats of water vapor and nitrogen results in 15 to 17 mass % extra nitrogen for flame extinguishment. Clearly, 35% water mist rather than 12 mass % would be needed in the absence of the latent and specific heat effects for the flame to be extinguished by oxygen dilution alone. It is interesting that the computer simulations show that the water extinction concentration (mass %) is about one third that of nitrogen. This is consistent with the thermodynamic argument made by Ndubizu et al. [7], which showed that the oxygen dilution effect is about one third of the total.

5.0   CONCLUSIONS

Computer simulations are performed to show extinction dynamics of a propane diffusion flame in co-flow geometry by monodispersed water droplets of extremely small size range (4 to 32 µm). At fixed drop size, as the mist concentration is increased to a critical value (extinction concentration), the flame lifts up from the burner rim and the flame blows-off. The simulations show that the water droplets entrained into the reaction kernel at the flame base play a critical role in extinguishing the flame. The computations show that the maximum rate of a chain-branching reaction inside the reaction kernel is reduced below a critical value at or above the extinction concentration. The critical reaction rate is about 5 times smaller than the maximum

reaction rate for the base case flame. The reaction forms OH and H radicals from O and H_2, and is used as an indicator for describing the extinction process. At mist concentrations below the extinction concentration, the maximum reaction rate is reduced by a factor of 2.5 only, and the flame is not extinguished. The droplet extinction concentration decreases from 15 to 10.5 mass % as the droplet size is increased from 4 to 32 μm. The large drops are found to penetrate reaction kernel at the flame base better than the small drops, and are more effective despite the decreased evaporation rate due to smaller surface to volume ratio. However, as the drop size is increased further, this trend reverses as the evaporation rates get too low for extinguishment of the flame.

6.0   ACKNOWLEDGEMENTS

7.0   REFERENCES

1. B.Z. Dlugogorski, R.K. Hichens, E.M. Kennedy, and J.W. Bozzeli, "Propagation of Laminar Flames in Wet Premixed Natural Gas-air Flames", Trans. Inst. Chem. Eng. B 76, 81 (1998)

2. G. Grant, J. Brenton, and D. Drysdale, "Fire Suppression by Water Sprays", Prog. Energy and Comb. Sci., 26, 79 (2000)

3. Rashbash, D.J., Rogowski, Z.W., and Stark, G.W.V., "Mechanism of Extinction of Liquid Fires with Water sprays", Combust. & Flame, 4, 223 (1960)

4. McCaffrey, B.J., "Jet Diffusion Flame Suppression Using Water Sprays- An Interim Report", Combust. Sci. & Tech., 40, 107 (1984); 63, 315 (1989)

5. G.G. Back, R.L. Darwin, and J.T. Leonard, "Full scale tests of water mist fire suppression systems for Navy shipboard machinery spaces", Proc. INTERFLAM 96, Cambridge, U.K., March 26-28 (1996)

6. Novozhilov, V., Harvie, D.J., Green, A.R., and Kent, "A Computational Fluid Dynamic Model of Fire Burning Rate and Extinction by Water Sprinkler", Combust. Sci. and Tech., 123, 227 (1997)

7. Ndubizu, C.C., Ananth, R., Tatem, P.A., and Motevalli, V., "On Water Mist Fire Suppression Mechanisms in a Gaseous Diffusion Flame", Fire Safety J., 31:253 (1998)

8. Ndubizu, C.C., Ananth, R., and Tatem, P.A., "The Effects of Droplet Size and Injection Orientation on Water Mist Suppression of Low and High Boiling Point Liquid Pool Fires", Combust. Sci. & Tech., 157, 63 (2000)

9. Prasad, K. Li, C., Kailasanath, K., Ndubizu C., Ananth, R., and Tatem, P.A., "Numerical Modeling of Water Mist Suppression of Methane-Air Diffusion Flames", Combust. Sci. & Tech., 32:325 (1998)

10. G.J. Liao, A.U. Modak, R.J. Kee, and J.-P. Delplanque, "Interaction of Small Water Droplets with a Methane Non-Premixed Jet Flame", Paper # H35, 5th U.S. Combustion Meeting, San Diego, CA, March 25-28 (2007)

11. K.C. Adiga, R. Adiga, and R.F. Hatcher, Jr., "Method and Device for Production, Extraction and Delivery of Mist with Ultrafine Droplets", U.S. Patent Number 6883724, April 26 (2005)

12. C.L. Beyler, "A Unified Model of Fire Suppression", J. Fire Protection Eng., 4, 5 (1992)

13. B. Downie, C. Polymeropoulos, and G. Gogos, "The Effects of Ventillation and Preburn Time on Water Mist Extinguishing of Diesel Fuel Pool fires", Fire Safety J., 24, 359 (1995)

14. K.C. Adiga, R,F, Hatcher Jr, R.S. Sheinson, F.W. Williams, and S. Ayers, "CFD Modeling Options for Total Flooding Behavior of Ultra Fine Water Mist", 16th Annual International Halon Options Technical Working Conference (HOTWC), Albuquerque, NM, May 16-18 (2006)

15. K.C. Adiga, R.F. Hatcher Jr, R.S. Sheinson, F.W. Williams, and S. Ayers, " A Computational and Experimental Study of Ultra fine Water Mist as a Total flooding Agent", J. Fire Safety, 42, 150 (2007)

16. K.C. Adiga, R.F. Hatcher Jr, E.W. Forsell, J.L. Scheffy, P.J. DiNenno, G.G. Back, J.P. Farley, and F.W. Williams, "Electronic Space Fire Protection: False Deck Mockup Fire Testing of Nanomist Systems", 15th Annual International Halon Options Technical Working Conference (HOTWC), Albuquerque, NM, May 23-26 (2005b)

17. Ravigururajan, T.S. and Betran, M.R., "A Model for Attenuation of Fire Radiation Through Water Droplets", Fire Safety J., 15, 171 (1989)

18. Ndubizu, C.C., Ananth, R., and Williams, F.W., "Water Mist Suppression of PMMA Boundary Layer Combustion – A Comparison of NanoMist and Spray Nozzle Performance", Memorandum Report, Naval Research Laboratory, Washington, DC, NRL/MR/6180-04-8824, September 20 (2004)

19. Ndubizu, C.C., Ananth, R., and Williams, F.W., "The Effects of Air-borne Water Mist on the Local Burning Rate of a PMMA Plate in Boundary Layer Combustion", Proceedings of the Halon Options Technical Working Conference (HOTWC), Albuquerque, NM, May 4-6, (2004)

20. Ndubizu, C.C., Ananth, R., and Williams, F.W., "Suppression and Extinguishment of Force-flow Boundary Layer Combustion by Ultra-fine Water Mist", Combust. Sci. and Tech., 179, 1867 (2007)

21. R. Ananth, C.C. Ndubizu, and F.W. Williams, "A Numerical Model for Water Mist Suppression of a solid Plate in Boundary Layer Flow", 14th Annual International Halon

Options Technical Working Conference (HOTWC), Albuquerque, NM, May 4-6, p. 1-10 (2004)

22. R. Ananth, C.C. Ndubizu, and P.A. Tatem, "Pyrolysis and Boundary Layer Combustion of a Non-Charring Solid Plate Under Forced Flow", Memorandum Report, Naval Research Laboratory, NRL/MR/6180-03-8700 (2003)

23. C.-H. Chen and J. Tien, "Diffusion Flame Stabilization at the Leading-Edge of a Fuel Plate", Combust. Sci. Tech., 50, 283 (1986)

24. A.M. Lentati and H.K. Chelliah, "Physical, Thermal, and Chemical Effects of fine-Water Droplets in Extinguishing Counterflow Diffusion Flames", Proc. Combust. Inst., 27:2839-2846 (1998)

25. A.M. Lentati and H.K. Chelliah, "Dynamics of Water Droplets in a Counterflow Field and their Effect on Flame Extinction", Combust.& Flame, 115, 158 (1998b)

26. Zegers, E.J., Williams, B.A., Sheinson, R.S., and Fleming, J.W., "Dynamics and Suppression Effectiveness of Monodisperse Water Droplets in Non-Premixed Counterflow Flames", 28th Int. Proc. Comb. Inst., 2931 (2000)

27. B.T. Fisher, A.R. Awtry, R.S. Sheinson, and J.W. Fleming, "Flow Behavior Impact on the suppression Effectiveness of Sub-10μm Water Drops in Propane/Air Coflow Non-Premixed Flames", 31st Int. Proc. Combust. Inst., 2731 (2006)

28. R. Ananth and R.C. Mowrey, "Ultra-Fine Mist Extinction of a Diffusion Flame", Paper # H34, 5th U.S. Combustion Meeting, San Diego, CA, March 25-28 (2007)

29. Shilling, H., Dlugogorski, B.Z., Kennedy, E.M., "Extinction of Diffusion Flames by Ultrafine Water Mist Doped with Metal Chlorides", Proc. of Sixth Australasian Heat and Mass Transfer Conference, December9-12, 275-282 (1996), Sydney, Australia. Also in Leonardi, E. and Madhusudana, C.V. (Eds), Begell House, New York, 275-282 (1998)

30. Linteris, G.T., Takahashi, F., and Katta, V.R., "Fuel Effects in Cup-Burner Flame Extinguishment", Paper#H21, 5th U.S. Combustion Meeting, San Diego, CA, March 25-28 (2007)

31. Z. Cheng, R.W. Pitz, and I.A. Wehrmeyer, "Lean and Ultralean Stretched Propane- Air Counter Flow Flames", Combust. & Flame, 145, 647 (2006)

32. Prasad, K., Li, C., Kailasanath, K., Ndubizu, C.C., Ananth, R., and Tatem, P.A., "Numerical Modeling of Methanol Liquid Pool Fires", Combustion Theory & Modeling, 3, 656 (1999)

33. Talbot, L, Cheng, R.K., Schefer, R.W., and Willis, D.R., "Thermophoresis of Particles in a Heated Boundary Layer", J. Fluid Mech., 101, 737 (1980)

34. Tseng, C.C. and Viskanta, R., "Enhancement of Water droplet Evaporation by Radiation Absorption", Fire Safety J., 41, 236-247 (2006)

35. Tseng, C.C. and Viskanta, R., "Absorptance and Transmittance of Water spray/Mist Curtains", Fire Safety J., 42, 106-114 (2007)

36. Sheinson, R.S., Penner-Hahn, J.E., and Indritz, D, "The Physical and Chemical Action of fire Suppressants", Fire Safety J., 15, 437 (1989)

37. I. Glassman, *Combustion*, Academic Press, London, (1987)

38. A. Coppalle and A. Vervische, "The Total Emissivities of High Temperature Flames", Combust. & Flame, 49, 101 (1983)

39. M.K. Denison, and B.W. Webb, J. Heat Transfer, 115, 1002 (1993)

40. Smith, T.F., Shen, Z.F., and Freidman, J.N., J. Heat Transfer, 104, 602 (1982)

41. Morsi, S.A. and Alexander, A.J., "An Investigation of Particle Trajectories in Two-phase Flow Systems", J. Fluid. Mech., 55, 193 (1972)

42. R.R. Bird, W.E. Stewart, E.N. Lightfoot, "Transport Phenomena", John Wiley & Sons, (1960)

43. M.A. Kanury, "Introduction to Combustion Phenomena", Gordon and Breach, New York (1977)

APPENDIX A – CONSERVATION EQUATIONS

The gas phase equations are a modification of the model given by Ananth et al. [21] to include the effects of multi-step chemistry, P-1 radiation, water mist, and co-flow geometry.

Continuity

$$\frac{\partial \rho}{\partial t} + \nabla.(\rho \vec{u}) = S_m \tag{A1}$$

momentum

$$\frac{\partial (\rho \vec{u})}{\partial t} + \nabla.(\rho \vec{u} \vec{u}) = -\nabla p - \nabla.\hat{\tau} + \rho \vec{g} + \vec{F}_d \tag{A2}$$

energy

$$\frac{\partial \rho E}{\partial t} + \nabla.(\vec{u}(\rho E + p)) = -\nabla.(\vec{q}_c + \vec{q}_r + \sum_i h_i \vec{J}_i) - \sum_i \frac{h_i^0}{M_i} R_i + S_h \tag{A3}$$

specie i conservation

$$\frac{\partial (\rho Y_i)}{\partial t} + \nabla.(\rho \vec{u} Y_i) = -\nabla.\vec{J}_i + R_i + S_i \tag{A4}$$

$$E = \sum_i Y_i h_i - \frac{p}{\rho} + \frac{\vec{u}^2}{2} \tag{A5}$$

$$h_i = \int_{T_{ref}}^{T} C_{pi} dT \tag{A6}$$

where ρ is the gas density. The quantities u is the velocity vector. Here, p is pressure, E is total energy density and Y_i is the mass fraction of ith specie. J_i is the diffusive flux of ith specie. R_i is net rate of change in the mass concentration of ith specie due to chemical reaction. q_c and q_r are conductive and radiative fluxes. τ is the stress tensor. g is the gravity vector. M_i is the molecular weight of specie i. h_i is the sensible enthalpy of specie i. h_{i0} is the enthalpy of formation of specie i at T_{ref}=298.15 K. T and T_{ref} are temperature and reference temperature of the gas. C_{pi} is the specific heat of specie i. S_m, F_d, S_h, S_i are coupling terms that represent contributions from the droplet phase, and are discussed later.

The cooling of the gas phase due to the water droplet evaporation is represented by S_h, which has opposite sign to the heat generation rate due to combustion in the energy equation (A3). The heat generation rate is represented by the second term on the right hand side of the energy equation. The water vapor dilutes the reactant concentrations and leads to lower reaction rates, R_i, and lower heat generation. The competition between the heat generation rate and the cooling rate by the droplets plays a critical role in the flame extinction phenomena.

A.1. *Transport Fluxes*

The conductive and radiative heat fluxes, shear stress, and diffusion mass flux depend on gradients, and are given by

$$\vec{q}_c = -\lambda_m \nabla T \tag{A7}$$

$$\vec{q}_r = -\xi \nabla G \tag{A8}$$

$$\hat{\tau} = \mu_m \left[(\nabla \vec{u} + \nabla \vec{u}^T) - \frac{2}{3} \nabla \cdot \vec{u} \hat{I} \right] \tag{A9}$$

$$\vec{J}_i = \rho D_{im} \nabla Y_i \tag{A10}$$

μ_m, λ_m are the viscosity and thermal conductivity of the gas mixture. D_{im} is the pseudo binary diffusivity of specie i in the gas mixture. I is the identity tensor. Superscript T refers to transpose of the vector. P-1 radiation model for the radiation flux may be used, where G is the incident radiation and ξ is the radiation parameter defined later.

A.2. *Chemical Reaction Rates*

The general form of rth reversible, reaction can be written as

$$\sum_{i=1}^{i=N} \upsilon'_{i,r} A_i \underset{k_{b,r}}{\overset{k_{f,r}}{\Longleftrightarrow}} \sum_{i=1}^{i=N} \upsilon''_{i,r} A_i \tag{A11}$$

where N is the total number of species, $\upsilon'_{i,r}$, $\upsilon''_{i,r}$ are stoichiometric coefficients of reactant i and product i in reaction r. A_i represents specie i. $k_{f,r}$ and $k_{b,r}$ are forward and backward reaction rate constants for the reaction r respectively. The net consumption/production rate of specie i is given by

$$R_i = M_i \sum_{r=1}^{N_R} \dot{R}_{i,r} \tag{A12}$$

$R_{i,r}$ is the volumetric reaction rate for the specie i appearing in r^{th} reaction, N_R is the number of reactions that the specie i participates in. The rate of rth reaction is given by

$$\dot{R}_{i,r} = (\upsilon''_{i,r} - \upsilon'_{i,r}) k_{f,r} \left[\prod_{j=1}^{N_r} [C_{j,r}]^{n'_{j,r}} - \frac{1}{K_r} \prod_{i=1}^{N_r} [C_{j,r}]^{n''_{j,r}} \right] \left[\sum_{j=1}^{N_r} \gamma_{j,r} C_j \right] \tag{A13}$$

N_r is the number of species in reaction r, $C_{j,r}$ is the mass concentration of each reactant and product species j in reaction r. $\eta'_{j,r}$ and $\eta''_{j,r}$ are the rate exponents for forward and backward reaction rates respectively for each reactant and product j in reaction r. K_r is the equilibrium reaction constant for reaction r. $\gamma_{i,r}$ is the third body efficiency of specie j in reaction r.

$$k_{f,r} = A_r T^{\beta_r} e^{-E_r/RT} \tag{A14}$$

A_r is the pre-exponential factor in the Arrhenius expression for the forward rate constant for reaction r. β_r and E_r are the exponent of the temperature and activation energy for the reaction r. R is the universal gas constant. The equilibrium constant for a reversible reaction is given by

$$K_r = \exp\left(\frac{\Delta S_r^0}{R} - \frac{\Delta H_r^0}{RT}\right)\left(\frac{P_{atm}}{RT}\right)^{\sum_{j=1}^{N_R}\left(v''_{j,r} - v'_{j,r}\right)} \tag{A15}$$

P_{atm} is atmospheric pressure.

$$\frac{\Delta S_r^0}{R} = \sum_{i=1}^{N}\left(v''_{i,r} - v'_{i,r}\right)\frac{S_i^0}{R} \tag{A16}$$

$$\frac{\Delta H_r^0}{R} = \sum_{i=1}^{N}\left(v''_{i,r} - v'_{i,r}\right)\frac{h_i^0}{R} \tag{A17}$$

S_i^0 and h_i^0 are the standard state entropy and enthalpy of formation of specie i. GRI3.0 database is used in evaluating the reaction rates.

A.3. *Mixture Properties*

The mixture properties are obtained from the individual specie properties using the kinetic theory of gases.

$$\rho = \frac{p}{RT\sum_i \dfrac{Y_i}{M_i}} \tag{A18}$$

$$\mu_m = \sum_i \frac{Y_i \mu_i}{\sum_j Y_i \phi_{ij}} \tag{A19}$$

$$\lambda_m = \sum_i \frac{Y_i \lambda_i}{\sum_j Y_i \phi_{ij}} \tag{A20}$$

$$\phi_{ij} = \frac{\left[1 + \left(\dfrac{\mu_i}{\mu_j}\right)^{1/2} \left(\dfrac{M_j}{M_i}\right)^{1/4}\right]^2}{\left[8\left(1 + \dfrac{M_i}{M_j}\right)\right]^{1/2}} \tag{A21}$$

$$D_{i,m} = \frac{1 - Y_i}{\displaystyle\sum_{j,j\neq i}\left(\dfrac{Y_j}{D_{ij}}\right)} \tag{A22}$$

$$C_{pm} = \sum_i Y_i C_{pi} \tag{A23}$$

μ_i, λ_i, C_{pi} are the viscosity, thermal conductivity, and specific heat of specie i. C_{pm} is the specific heat of the gas mixture. D_{ij} is the binary diffusion coefficient for species i and j.

A.4. *Individual Specie Properties*
Chapman-Enskog equation for viscosity is given by

$$\mu_i = 2.67x10^{-6} \frac{\sqrt{M_i T}}{\sigma_i^2 \Omega_{\mu,i}} \tag{A24}$$

$$T_i^* = \frac{T}{\left(\varepsilon_l / \kappa_B\right)_i} \tag{A25}$$

Eucken Equation for the thermal conductivity is given by

$$\lambda_i = \left(C_{pi} + \frac{5}{4}\frac{R}{M_i}\right)\mu_i \tag{A26}$$

Chapman-Enskog equation for binary diffusivities

$$D_{ij} = 0.0188 \frac{\left[T^3 \left(\dfrac{1}{M_i} + \dfrac{1}{M_j} \right) \right]^{1/2}}{p \sigma_{ij}^2 \Omega_{Dij}} \tag{A27}$$

$$\sigma_{ij} = \frac{1}{2} \left(\sigma_i + \sigma_j \right) \tag{A28}$$

where the diffusion collision integral, Ω_{Dij}, is a function of $T_{ij}{}^*$, which is given by

$$T_{ij}^* = \frac{T}{\sqrt{\left(\varepsilon_l / \kappa_B \right)_i \left(\varepsilon_l / \kappa_B \right)_j}} \tag{A29}$$

σ_i and ε_l are Lennard-Jones parameters given by GRI 3.0 property database and K_B is the Boltzmann constant. Piecewise polynomials are used for specific heat, C_{pi}, of individual specie i. A and B are empirical coefficients given by GRI 3.0 property database.

For $T_{min,1}(200\ \text{K}) < T < T_{max,1}$ (1000 K)

$$C_{pi}(T) = A_{1,i} + A_{2,i} T + A_{3,i} T^2 + A_{4,i} T^3 + A_{5,i} T^4 \tag{A30}$$

For $T_{min,2}$ (1000 K)$< T < T_{max,2}$ (3500 K)

$$C_{pi}(T) = B_{1,i} + B_{2,i} T + B_{3,i} T^2 + B_{4,i} T^3 + B_{5,i} T^4 \tag{A31}$$

A.5. *Radiation Equations*
The conservation equation for radiation, G is given by

$$\nabla.(\xi \nabla G) + 4\pi (a \frac{\sigma T^4}{\pi} + E_p) - (a + a_p) G = 0 \tag{A32}$$

The radiation parameter, ξ, is defined as

$$\xi = \frac{1}{3(a + a_p + \sigma_p)} \tag{A33}$$

$$\sigma_p = \sum_{n=1}^{N_p} (1 - f_{pn})(1 - \varepsilon_{pn}) A_{pn} \tag{A34}$$

$$E_p = \sum_{n=1}^{N_p} \varepsilon_{pn} A_{pn} \frac{\sigma T_{pn}^4}{\pi} \tag{A35}$$

$$a_p = \sum_{n=1}^{N_p} \varepsilon_{pn} A_{pn} \tag{A36}$$

$$A_{pn} = \frac{\pi d_{pn}^2}{4} \tag{A37}$$

a is the gas absorption coefficient, σ is the Stefan-Boltzmann constant. σ_p, E_p, a_p are the equivalent scattering factor, equivalent emissivity, and equivalent absorption coefficient for the droplet phase. f_{pn}, ε_{pn}, A_{pn}, d_{pn}, and T_{pn} are the isotropic scattering factor, emissivity, projected area, diameter, and temperature of the nth droplet. N_p is the number density, which is the number of water droplets contained in a unit gas volume.

Despite the radiation field is thermally thin for the soot less diffusion flame, we used P-1 model for computational simplicity. Also, radiation does not play a critical role in flame extinction because of the small geometry (1.25 cm radius flame). Furthermore, as discussed in the theory section of the paper, the droplet contribution to the radiation field is small especially near the base of the flame mainly due to small length scales of the co-flow burner and extremely small droplet sizes. This is confirmed by preliminary computations, which included the droplet contribution with ε_{pn}=0.35 and σ_p=0.5. The preliminary computations for 8 μm drops showed that the droplet radiation has only a minimal ($<$ 15%) effect on the computed extinction concentrations. Hence, we set ε_{pn} =σ_p=0, and neglect both the radiation effects on droplet evaporation and the droplet effects on radiation field in the gas phase for all of the computations shown in this paper.

Weighted sum gray gas model (WSGGM) is used to calculate emissivity and the absorption coefficient for the gas as functions of composition and temperature.

$$\varepsilon = \sum_{i=0}^{I} a_{\varepsilon,i} \left(1 - e^{-\kappa_i ps}\right) \tag{A38}$$

$a_{\varepsilon,i}$ and κ_i are the emissivity weighting factors and absorption coefficients for the ith fictitious gray gas. $a_{\varepsilon,i}$ are polynomial functions of temperature and are given in [38-40] along with the values of κ_i for the absorbing gray gas species. p is sum of partial pressures of absorbing gray gas species (CO_2 and H_2O) and s is the characteristic cell size. The absorption coefficient of the gases is given by

$$a = \frac{-\ln(1 - \varepsilon)}{s} . \tag{A39}$$

A.6.   *Coupling Terms*

The mass exchange between droplet and gas phases due to the evaporation of droplets is given by

$$S_m = \sum_{n=1}^{N_p} \frac{dm_{pn}}{dt} \tag{A40}$$

The mass exchange affects both ρ and X, and leads to oxygen dilution and specific heat effects. The evaporation rate is summed over all the droplets in unit volume of gas, m_{pn} is the droplet mass. N_p is related to the mass fraction of the droplets, X_w, by

$$X_w = \sum_{n=1}^{N_p} \frac{\pi \rho_p}{6\rho} d_{pn}^3 \tag{A41}$$

ρ_p is the liquid water density. At the air inlet, the number density, N_{p0}, and the mass fraction of the monodispersed water drops, X_{w0}, can be directly related

$$N_{p0} = \frac{6X_{w0}\rho}{\pi d_{pn}^3 \rho_p} \tag{A42}$$

$$F_d = \sum_{n=1}^{N_p} m_{pn} \left[\frac{3\mu C_{Dn} \operatorname{Re}_{pn}(u_{pn} - u)}{4\rho_p d_{pn}^2} \right] \tag{A43}$$

u_{pn} and u are the droplet and gas velocity vectors. C_{Dn} is the droplet drag coefficient, which is a function (polynomial) of the droplet Reynolds number, C_{Dn}.is given by Morsi et al, [41] for Re_{pn} < 1. The drag term affects the degree of droplet entrainment into the flame. The drag coefficient is given by

$$C_{Dn} = a_1 + \frac{a_2}{\operatorname{Re}_{pn}} + \frac{a_3}{\operatorname{Re}_{pn}^2} \tag{A44}$$

a_1 to a_3 are polynomial coefficients given in Morsi, et al., [41]. The Reynolds number, Re_{pn}, is based on the magnitude of the droplet velocity vector relative to the gas, and is given by

$$\operatorname{Re}_{pn} = \frac{\rho d_{pn} |u - u_{pn}|}{\mu_m}. \tag{A45}$$

The energy exchange due to evaporation of the droplets is given by

$$S_h = \sum_{n=1}^{N_p} \left[\frac{\pi}{6} d_{pn}^3 \rho_p C_{pd} \frac{dT_{pn}}{dt} + \left(-h_{fg} + \int_{T_{ref}}^{T_{pn}} C_{p,H2O} dT \right) \frac{dm_{pn}}{dt} \right] \tag{A46}$$

The energy exchange includes the sensible heat absorption due to droplet heating, and the latent heat absorption due to droplet evaporation. T_{pn} and C_{pd} are the temperature and specific heat of the droplet. $C_{p,H2O}$ and h_{fg} are the specific heat of water vapor and latent heat of vaporization of water respectively.

$$S_i = S_m \quad \text{for } i=H_2O \tag{A47}$$

$$S_i = 0 \quad \text{for } i \neq H_2O \tag{A48}$$

A.7. *Lagrangian Droplet Equations*

Thr rate of evaporation of nth droplet is defined as

$$\overset{\bullet}{m}_{pn} = \frac{dm_{pn}}{dt} \tag{A49}$$

The x-component of the force balance on the nth droplet is given by

$$\frac{du_{pnx}}{dt} = \frac{3\mu C_{Dn} \operatorname{Re}_{pn}}{4\rho_p d_{pn}^2}\left(u_x - u_{pnx}\right) - \frac{g(\rho_p - \rho)}{\rho_p} \tag{A50}$$

The first term on the right hand side of equation (A50) represents the drag force exerted by the gas phase on the droplet. The second term on the right hand side of equation (A50) represents the effect of gravity on the droplet. Equation (A50) shows that the gravity effects become less significant compared to the drag force as the droplet diameter decreases. The r-component of the force balance for the nth droplet is given by

$$\frac{du_{pnr}}{dt} = \frac{3\mu C_{Dn} \operatorname{Re}_{pn}}{4\rho_p d_{pn}^2}\left(u_r - u_{pnr}\right) \tag{A51}$$

The droplet trajectories for the nth droplet is defined by

$$\frac{dx_{pni}}{dt} = u_{pni} \quad \text{for } i=x \text{ or } r \text{ and } n=1, N_p \tag{A52}$$

u_{pnx} and u_{pnr} are the x and r components of the droplet velocities respectively. u_x and u_r are the x and r components of the gas velocities. -The energy balance for the droplet is given by

$$m_{pn}C_{pd}\frac{dT_{pn}}{dt} = h_{pn}\pi d_{pn}^2\left(T - T_{pn}\right) + h_{fg}\overset{\bullet}{m}_{pn} + \sigma\pi d_{pn}^2\varepsilon_{pn}\left(\theta_R^4 - T_{pn}^4\right) \tag{A53}$$

h_{pn} is the heat transfer coefficient for the droplet. T is the gas temperature, and θ_R is the radiation temperature. The term on the left hand side of equation (A53) represents the sensible heat

absorption due to droplet heating. The first term on the right hand side of equation (A53) represents the conductive and convective heat transport to the droplet surface from the gas phase and is based on Newton's law of cooling with a characteristic heat transfer coefficient. The second term on the right hand side of equation (A53) represents the evaporative cooling of the droplet. The third term on the right hand side of equation (A53) is the net radiation heat flux to the surface of the droplet, where

$$\theta_R = \left[\frac{G}{4\sigma}\right]^{1/4}.$$
(A54)

The incident radiation G is given by the solution of equation (A32). It was found that the radiation increases T_{pn} significantly but does not lead to evaporation at 100 % humidity, as one might have expected. This is because of zero water vapor concentration gradient between the droplet surface and the bulk air. Therefore, the radiation effects on droplet evaporation rate are neglected by setting $\varepsilon_{pn} = 0$ in equation (A53) for all the computations shown in this paper.

Nusselt number, Nu_{pn}, is given by the usual laminar boundary-layer equation [42] for spherical particles,

$$Nu_{pn} = \frac{h_{pn}d_{pn}}{k} = 2.0 + 0.6\,Re_{pn}^{1/2}\,Pr^{1/3}.$$
(A55)

Pr and k are the Prandtl number and thermal conductivity of the gas respectively. The first and second terms on the right hand side of equation (A55) are due to conduction and convection heat transfer in the gas phase respectively.

Equations (A49-A53) contain six unknowns, and an additional equation is needed to obtain a solution. In general, the additional equation is obtained by considering mass transfer rate of water vapor from the droplet to the gas phase. However, approximations to the mass transfer rate can be made at droplet temperatures below ambient and near boiling point for computational implementation as discussed below.

The evaporation rate of the droplet is neglected for droplet temperature below a minimum temperature T_{vap}=287 K.

$$\dot{m}_{pn} = 0 \ \text{for} \ T_{pn} < T_{vap}$$
(A56)

The evaporation rate is affected by mass transfer of water vapor from the droplet surface into the gas phase for droplet temperatures in between T_{vap} and the boiling point T_b.

$$\dot{m}_{pn} = k_{cn}\pi d_{pn}^2 \left(C_{H2O,s} - C_{H2O,n}\right) \ \text{for} \ T_{vap} < T_{pn} < T_b$$
(A57)

$$C_{H2O,s} = \frac{P_{sat}}{RT_{pn}} \tag{A58}$$

$$Sh_{pn} = \frac{k_{cn}d_{pn}}{D_{i,m}} = 2.0 + 0.6\,\mathrm{Re}_{pn}^{1/2}\,Sc^{1/3} \tag{A59}$$

k_{cn} is the mass transfer coefficient and is given by Sherwood number, which follows equation A(59). $C_{H2O,s}$ is the thermodynamic equilibrium concentration of water vapor at droplet temperature T_{pn}. $C_{H2O,s}$ depends on saturation water vapor pressure, P_{sat}, through ideal gas law and P_{sat} depends exponentially on T_{pn}. $C_{H2O,n}$ is the water vapor concentration in the gas phase.

For droplet temperatures close to the boiling point of water, mass transfer resistance for water vapor has negligible effect. Therefore, the droplet temperature is set to T_b in equation (A53), and the droplet achieves steady state. The left hand side of equation (A53) is set to zero and rearranged to obtain an explicit expression for the evaporation rate as shown below.

$$\dot{m}_{pn} = \frac{2\pi d_{pn}}{h_{fg}}\left[k\left(1 + 0.23\,\mathrm{Re}_{pn}^{1/2}\right)(T - T_b) + 0.5\varepsilon_{pn}d_{pn}\sigma\left(\theta_R^4 - T_b^4\right)\right] \text{ for } T_{pn} \approx T_b \tag{A60}$$

The first and second terms within the square parentheses on the right hand side of equation (A60) represent conduction and convection heat transfer and radiation heat transfer respectively. As the droplet diameter gets small, the radiation term and the convective term containing Re_{pn} get small compared to the conduction term. However, the radiation term is neglected in the computations shown in this paper as discussed earlier. The conduction term in equation (A60) is equivalent to the well known d^2-law [43] in the limit $B = C_p(T-T_b)/h_{fg} \ll 1$, which is 0.33 for water droplet.